

Bachelor Thesis

Gamma-Ray Flux from Decay of
Aluminum-26 and Iron-60 inside the Local Bubble

Niklas Bauer

Würzburg, June 2023



Julius-Maximilians-Universität Würzburg
Faculty of Physics and Astronomy

Supervisor: Dr. Thomas Siebert

Abstract

Context: The 1809 keV gamma-ray line of the Milky Way (MW) as it is seen by COMPTEL shows the abundance of ^{26}Al in the Galaxy. Large-scale structures imply that there could be an isotropic foreground. The Local Bubble (LB) is a candidate for this since in it there have been two supernovae (SNe) in the last 8 Myr.

Aims: ^{26}Al and ^{60}Fe enter the interstellar medium (ISM) as yields of massive stars. The goal of this thesis is to understand the abundance of these isotopes and calculate the expected gamma-ray line emission of the LB for the ^{26}Al 1809 keV line and for the two ^{60}Fe lines with 1173 keV and 1332 keV, filled with the yields of two SNe.

Methods: For this, the Hydrostatic equilibrium and nuclear reactions in stars are described. Nucleosynthesis leading to these isotopes, ^{26}Al and ^{60}Fe with half-lives of $7.17 \cdot 10^5$ yr and $2.60 \cdot 10^6$ yr is also shown and how these isotopes are then transported into the ISM. Using Pacific Ocean crust measurements the mass of ^{60}Fe ejecta in the mentioned SNe is obtained. The progenitor star masses are determined using the stellar evolution models with metallicities in the range of $(\text{Fe}/\text{H}) = ((-0.9) - (-0.3))$ as well as rotational velocities of heavy stars in the range of $v = (30 - 240) \text{ km s}^{-1}$. A model based on line-of-sight integration is developed and the radioactive decay is translated into an emissivity profile, adding a time evolution with the respective ages of the SNe.

Results: Given the possible masses of the progenitor stars with $M_{\text{Star}} = (13 - 25) M_{\odot}$ the yields range between $M_{^{26}\text{Al}} = ((1.55 - 13.7) \cdot 10^{-5} M_{\odot})$ and $M_{^{60}\text{Fe}} = ((0.8 - 50) \cdot 10^{-6} M_{\odot})$. From line of sight integration and for different positions of the SNe model expected flux for the two isotopes we find a total integrated all-sky 1809 keV line flux

$F_{\text{Al}26} = ((0.73 - 6.4) \cdot 10^{-6} \text{ ph cm}^{-2} \text{ s}^{-1})$ and 1173/1332 keV line fluxes

$F_{\text{Fe}60} = ((0.45 - 22) \cdot 10^{-7} \text{ ph cm}^{-2} \text{ s}^{-1})$. With an isotropic fraction of 50% for the 1809 keV gamma-ray line flux and 54% for the 1173/1332 keV line fluxes.

Conclusions: Simulations with the model expected all-sky emission for the future COSI-SMEX mission result in no significant detection of the LB to the Galactic background, within the 2-year planned observation time.

Zusammenfassung

Kontext: Die Kartierung der Milchstraße durch COMPTEL in der Gammastrahlen Linie 1809 keV zeigt das Vorkommen von ^{26}Al . Größere Strukturen weisen auf einen isotropen Vordergrund hin. Die Lokale Blase (LB) ist ein Kandidat für einen isotropen Beitrag, da in ihr zwei Supernovae (SNe) in den letzten 8 Myr statt gefunden haben.

Ziele: ^{26}Al und ^{60}Fe gelangen als Ejekta massereicher Sterne in das interstellare Medium (ISM). Das Ziel dieser Arbeit ist es, die Häufigkeit dieser Isotope zu verstehen und die erwartete Gammastrahlenemission der LB für die ^{26}Al -Linie mit 1809 keV und für die beiden ^{60}Fe -Linien mit 1173 keV und 1332 keV zu berechnen.

Methoden: Hierfür werden das hydrostatische Gleichgewicht und Kernreaktionen in Sternen beschrieben. Die Nukleosynthese, die zu diesen Isotopen, ^{26}Al und ^{60}Fe mit Halbwertszeiten von $7.17 \cdot 10^5$ yr und $2.60 \cdot 10^6$ yr führt, wird ebenfalls gezeigt und wie diese Isotope dann in das ISM transportiert werden. Anhand von Ozeankruste Messungen im Pazifik wird die Masse der ^{60}Fe -Ejekta in den genannten SNe ermittelt. Die Massen der SNe Vorläufersterne werden mit Hilfe von Sternentwicklungsmodellen und Metallizitäten im Bereich von $(\text{Fe}/\text{H}) = ((-0.9) - (-0.3))$ sowie Rotationsgeschwindigkeiten schwerer Sterne im Bereich von $v = (30 - 240) \text{ km s}^{-1}$ abgeschätzt. Ein Modell basierend auf Sichtlinienintegration ist entwickelt und mit einem Emissivitätsprofil auf der Basis des radioaktiven Zerfalls und dem jeweiligen Alter der SNe gefüllt.

Ergebnisse: Bei den möglichen Sternmassen von $M_{\text{Star}} = (13 - 25) M_{\odot}$ liegen die Ejekta zwischen $M_{^{26}\text{Al}} = ((1.55 - 13.7) \cdot 10^{-5} M_{\odot})$ und $M_{^{60}\text{Fe}} = ((0.8 - 50) \cdot 10^{-6} M_{\odot})$. Aus der Sichtlinienintegration und für verschiedene Positionen der SNe wird der gesamt Gammastrahlen Fluss der beiden Isotope bestimmt und ergibt in 1809 keV

$F_{\text{Al}26} = ((0.73 - 6.4) \cdot 10^{-6} \text{ ph cm}^{-2} \text{ s}^{-1})$ und in 1173/1332 keV

$F_{\text{Fe}60} = ((0,45 - 22) \cdot 10^{-7} \text{ ph cm}^{-2} \text{ s}^{-1})$. Mit einem isotropen Anteil von 50% für den 1809 keV-Gammastrahlenfluss und 54% für den 1173/1332 keV-Gammastrahlenfluss.

Schlussfolgerungen: Simulationen mit dem erwarteten Gesamtfluss für die künftige COSI-SMEX-Mission führen zu keinem signifikanten Nachweis der LB zum galaktischen Hintergrund innerhalb der 2-jährigen Beobachtungszeit.

Contents

1. Introduction	1
2. Stellar Evolution	4
2.1. Stellar Structure Equations	4
2.2. Nuclear Burning	5
2.3. Supernovae	7
2.4. Nucleosynthesis Yields	9
3. Local Bubble	11
3.1. Introduction to Superbubbles	11
3.2. Morphology of the Local Bubble	11
3.3. Pacific Ocean Crust Fe60 Abundance	15
4. Gamma Ray Flux Expectations	17
4.1. Line of Sight inside of the Local Bubble	17
4.2. Gamma-Ray Emission from decaying Isotopes	18
4.2.1. Radioactive decay of Al26 and Fe60	18
4.2.2. Numerical Examples	21
4.2.3. Constellations for SNe	22
4.3. Calibration of the Supernova-Mass	23
4.3.1. Rotational velocity	23
4.3.2. Metallicity	25
4.3.3. Estimated Aluminum 26 Yields	26
4.3.4. Extrapolation to supersolar Metallicities	28
4.4. Expected Gamma-Ray All-Sky Images	32
4.4.1. Distant Superbubble	36
5. Simulations for the Compton Spectrometer and Imager Satellite Mission	38
5.1. Compton Spectrometer and Imager	38
5.2. Simulations	39
5.3. Simulation Results	41
6. Discussion	43
6.1. Direct Comparison to Aluminum 26 MW Map	43

6.2. Cosmic Gamma Ray Background Lines	44
7. Conclusion	46
A. Appendix	51
A.1. Model Programming	51
A.2. Additional Figures	54

1. Introduction

Modern astrophysical measurements aim to combine information that is obtained for different parts of the electromagnetic spectrum. This is called multiwavelength astronomy. One regime that lacks behind in the currently explored spectrum is the soft gamma-ray regime. To fill this gap the Compton Spectrometer and Imager (COSI) a small explorer mission (SMEX) is set to start in 2027. This satellite will collect data in the range of 0.2-5.0 MeV. [Tomsick et al., 2019] A process that leads to gamma rays in this range is the beta-decay of radioactive nuclei. The products of beta decay often are isotopes in an excited state, emitting gamma rays going into the ground state. Two isotopes contributing to gamma rays in this energy range are ^{26}Al (with a gamma-ray line at 1809 keV) and ^{60}Fe (with gamma-ray lines at 1173 keV and 1332 keV). The ^{26}Al has first been measured by COMPTEL [Diehl et al., 1995]. (See Fig. 1.1)

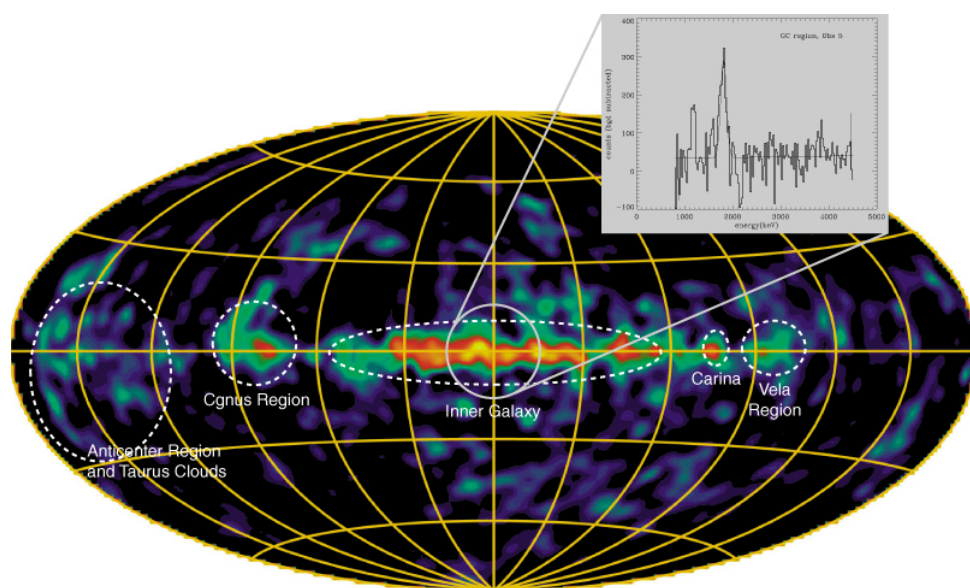


Figure 1.1.: The all-sky map from COMPTEL at energy 1.8 MeV. Also the spectrum for the central region of the Galaxy is shown. Figure taken from https://heasarc.gsfc.nasa.gov/docs/cgro/cgro/comptel_al26.html

The respective spectrum has then been measured by INTEGRAL/SPI over an observation time of nearly 18 years and is shown in Fig. 1.2.

In addition to the ^{26}Al , INTEGRAL/SPI also measured the ^{60}Fe in both of the characteristic gamma-ray lines at 1173 keV and 1332 keV [Wang et al., 2007]. All these components add to the cosmic gamma-ray background (CGB). The CGB is known since its discovery

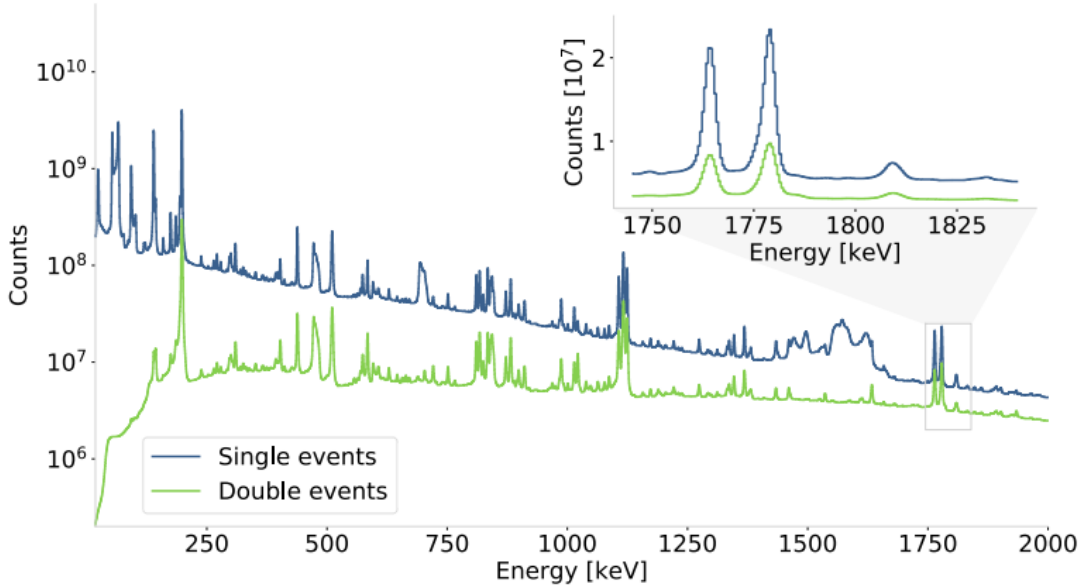


Figure 1.2.: Spectrum for the counts of the INTEGRAL/SPI measurement as used in [Pleitinger et al., 2023]. In the inset the characteristic gamma-ray line for the ^{26}Al at 1.809 keV is recognizable even though dominated by ^{28}Al and ^{214}Bi gamma-ray lines at 1779 and 1764 keV.

with the *SAS* – 2 satellite and is one of the most fundamental observables in the gamma-ray astronomy [Inoue, 2014]. Various gamma-ray emitting sources are candidates for this background radiation such as blazars, star-forming galaxies, radio galaxies, gamma-ray bursts, but also nucleosynthesis and radioactive decay. Therefore it is possible to have gamma-ray lines from the latter in the CGB. These might not be a background component but a foreground contribution. Within the last 8 Myr, two supernovae (SNe) happened in the vicinity of the Solar System. Therefore it is possible that the Solar System is embedded in the gamma-ray glow from these SNe, considering that the lifetimes of ^{26}Al is 1 Myr and ^{60}Fe is about 3.75 Myr. As previous studies suggest there could be a significant foreground emission in ^{26}Al ([Siegert et al., 2022]).

In this work we investigate the possibility that this foreground might be related to the Local Bubble (LB), the superbubble that surrounds our Solar System. For this, it is of interest to understand the origin, the occurrence, and the resulting gamma rays of the two isotopes. To simulate these properties a model is designed based on the LB. Inside this model, different gamma-ray emitting events can be placed and via the use of a profile, the resulting gamma-ray emissivity in every bin is determined leading to a flux for the different isotopes via line of sight integration. To get a probable value of the luminosity for each event, it is needed to classify the event. For the two SNe that reached our solar system ≈ 7 Myr and ≈ 3 Myr ago, evidence for radioactive isotopes is provided by samples from the Pacific Ocean crust [Chaikin et al., 2022]. To determine the starting condition assumptions for the metallicity and the rotational velocity of the preexisting stars are

made and gauged with Pacific Ocean crust measurements giving information about the amount of ^{60}Fe that reached us. This thesis is structured as follows:

In Chp. 2 the stellar evolution is displayed, then in Chp. 3 the physics of superbubbles and the Local Bubble are described. In Chp. 4 The expected gamma-ray line fluxes are modeled before we then simulate these flux images in Chp. 5 for the COSI instrument. At last, we discuss in Chp. 6 the results and conclude the information given in the following in Chp. 7.

2. Stellar Evolution

2.1. Stellar Structure Equations

To describe the origin of radioactive nuclei, we must understand the physical state of a star in general and, in addition, the various processes that lead to the production of the different elements.

The physical principle in massive stars consists of a combination of radiation, ideal gas, and degenerate electrons that build up the necessary pressure, $P(r)$ to counteract gravity. For this to be in a hydrostatic equilibrium the pressure needs to be

$$\frac{dP}{dr} = -G M(r) \rho(r) r^{-2} \quad (2.1)$$

with $M(r)$ being the interior mass, G being the gravitational constant, and $\rho(r)$ being the density at a given radius r within the star. With the mass continuity equation:

$$\frac{dM}{dr} = 4\pi r^2 \rho \quad (2.2)$$

If ρ is assumed, to zero order, to be constant within the star, integration of eq. 2.2 gives the proportionality:

$$\rho \propto \frac{M}{R^3} \quad (2.3)$$

And for a small radius, the hydrostatic equilibrium (eq. 2.1) becomes:

$$P_C \propto \frac{M\rho}{R_S} \quad (2.4)$$

Where P_C is the central pressure and R_S is the stellar radius. When the relation (2.3) is inserted in (2.4) it reads:

$$P_C \propto \frac{M^2}{R_S^4} \quad (2.5)$$

For an ideal gas, the equation of state gives:

$$P \propto \frac{\rho T}{\mu} \quad (2.6)$$

Where T is the temperature and μ is the mean molecular weight. For this (2.6) inserted

in (2.5) then one obtains:

$$T_C \propto \frac{\mu M}{R} \quad (2.7)$$

This equation shows the basic relation between the temperature in the core T_c , the Mass M , and the stellar radius R_S [Lugaro and Chieffi, 2011].

The energy that a star loses by radiation is produced by nuclear reactions. These nuclear reactions depend strongly on the temperature, as they can produce higher-order nuclei only at higher temperatures. With this and the temperature mass relation (2.7), massive ($>8\odot$) stars are the main producers of high-order elements [Siegert, 2017].

2.2. Nuclear Burning

The different nuclear reactions in stars can be divided into different burning phases. With about 90 % of their lifetime, stars spend most of their time burning hydrogen. Two processes that produce alpha particles out of protons are the pp chain and the CNO cycle. The pp chain starts at temperatures of ≈ 10 MK. It begins with p and p fusion and builds up through a sequence of proton captures and β decays [Lugaro and Chieffi, 2011]. In Tab. 2.1 these processes are shown. The mass defect for a process is the energy Q_{tot} that is released in these processes and is also displayed in Tab. 2.1. The CNO cycle is the next energetic process, burning protons to alpha particles. Due to a high coulomb barrier, this process starts at higher temperatures than the pp chain with ≈ 20 MK. The first reaction in the CNO cycle is the proton capture of carbon. The resulting nitrogen then decays via β decay back into a carbon isotope with now a higher nucleon count, again and again. If you look at table 2.1 it becomes clear why we talk about a cycle. We begin with e.g. ^{12}C plus a proton and go through the reactions until we end up with ^{12}C this time plus an α particle. At $\approx 25 - 30$ MK also oxygen is produced and the cycle is fully enabled. At $\approx 40 - 50$ MK proton captures of the high order nuclei in the former processes form neon and sodium isotopes which build the NeNa cycle. If the temperature rises further the sodium not only decays into neon but forms magnesium. With ≈ 60 MK the equilibrium abundances of all isotopes between ^{20}Ne up to ^{27}Al are reached and the complete NeNaMgAl sequence is intact [Lugaro and Chieffi, 2011].

The focus of this work will be on intermediate lifetime isotopes. For these isotopes, we need to understand the production, destruction, and ejection from massive stars. One of these isotopes is produced in the NeNaMgAl sequence: ^{26}Al . It arises with the proton capture of a ^{25}Mg . Due to its half-life of $7.17 \cdot 10^5$ yr it can be ejected into the ISM through stellar winds and during supernova explosions, and is therefore a good marker for nucleosynthesis in stars and the abundance of these stars. The second abundant isotope

reaction	Q_{tot} [MeV]
pp chain (≥ 10 MK)	
$p + p \rightarrow d + e^+ + \nu$	1.442
$d + p \rightarrow {}^3\text{He}$	5.494
${}^3\text{He} + {}^3\text{He} \rightarrow {}^4\text{He} + 2p$	12.860
${}^3\text{He} + {}^4\text{He} \rightarrow {}^7\text{Be}$	1.587
${}^7\text{Be} + e^- \rightarrow {}^7\text{Li} + e^+ + \nu$	0.862
${}^7\text{Be} + p \rightarrow {}^8\text{B} \rightarrow {}^8\text{Be} + e^+ + \nu$	
$\rightarrow \alpha + \alpha$	18.209
${}^7\text{Li} + p \rightarrow {}^8\text{Be} \rightarrow \alpha + \alpha$	17.347
CNO cycle (≥ 20 MK)	
${}^{12}\text{C} + p \rightarrow {}^{13}\text{N}$	1.944
${}^{13}\text{N} \rightarrow {}^{13}\text{C} + e^+ + \nu$	2.220
${}^{13}\text{C} + p \rightarrow {}^{14}\text{N}$	7.551
${}^{14}\text{N} + p \rightarrow {}^{15}\text{O}$	7.297
${}^{15}\text{O} \rightarrow {}^{15}\text{N} + e^+ + \nu$	2.754
${}^{15}\text{N} + p \rightarrow {}^{12}\text{C} + \alpha$	4.966
${}^{15}\text{N} + p \rightarrow {}^{16}\text{O}$	12.127
${}^{16}\text{O} + p \rightarrow {}^{17}\text{F}$	0.600
${}^{17}\text{F} \rightarrow {}^{17}\text{O} + e^+ + \nu$	2.761
${}^{17}\text{O} + p \rightarrow {}^{14}\text{N} + \alpha$	1.192
${}^{17}\text{O} + p \rightarrow {}^{18}\text{F}$	5.607
${}^{18}\text{F} \rightarrow {}^{18}\text{O} + e^+ + \nu$	1.656
${}^{18}\text{O} + p \rightarrow {}^{15}\text{N} + \alpha$	3.981
${}^{18}\text{O} + p \rightarrow {}^{19}\text{F}$	7.994

reaction	Q_{tot} [MeV]
NeNaMgAl sequence (≥ 40 MK)	
${}^{20}\text{Ne} + p \rightarrow {}^{21}\text{Na}$	5.979
${}^{21}\text{Na} \rightarrow {}^{21}\text{Ne} + e^+ + \nu$	3.548
${}^{21}\text{Ne} + p \rightarrow {}^{22}\text{Na}$	6.739
${}^{22}\text{Na} \rightarrow {}^{21}\text{Ne} + e^+ + \nu$	2.842
${}^{22}\text{Ne} + p \rightarrow {}^{23}\text{Na}$	8.794
${}^{23}\text{Na} + p \rightarrow {}^{20}\text{Ne} + \alpha$	2.377
${}^{23}\text{Na} + p \rightarrow {}^{24}\text{Mg}$	11.693
${}^{24}\text{Mg} + p \rightarrow {}^{25}\text{Al}$	6.548
${}^{25}\text{Al} \rightarrow {}^{25}\text{Mg} + e^+ + \nu$	4.277
${}^{25}\text{Mg} + p \rightarrow {}^{26}\text{Al}$	6.307
${}^{26}\text{Al} \rightarrow {}^{26}\text{Mg} + e^+ + \nu$	4.004
${}^{26}\text{Al} + p \rightarrow {}^{27}\text{Si}$	12.275
${}^{26}\text{Mg} + p \rightarrow {}^{27}\text{Al}$	8.271
${}^{27}\text{Si} \rightarrow {}^{27}\text{Al} + e^+ + \nu$	4.812
${}^{27}\text{Al} + p \rightarrow {}^{28}\text{Si}$	11.585
${}^{27}\text{Al} + p \rightarrow {}^{24}\text{Mg} + \alpha$	1.601

Table 2.1.: "Hydrogen burning" nucleosynthesis processes in stars. Processes result in the abundance of elements from hydrogen up to silicon. Every reaction has also an energy balance, which equals the mass defect comparing the two sides of the processes, given as Q_{tot} as shown in [Lugaro and Chieffi, 2011]

we examine is ^{60}Fe with a half-life of $2.60 \cdot 10^6$ yr. ^{60}Fe is only produced in the neutron-rich environment of SNe.

For massive stars, even higher temperatures can be reached, allowing additional burning phases. This happens when the star leaves the phase of central H burning. This is the case when all the hydrogen in the central region is burned and the increasing pressure leads to higher temperatures. At ≈ 100 MK the triple- α Helium burning starts, where two α particles connect and form ^8Be . As shown in Tab. 2.2, for this process Q_{tot} is negative and no energy is released. ^8Be is not stable and therefore catches the third α -particle to get to the stable isotope ^{12}C . This process, then again, adds up to the total energy of the star. Stars with masses higher than about $8 M_{\odot}$ can also perform neon burning ($T \gtrsim 120$ MK), oxygen burning ($T \gtrsim 150$ MK), carbon burning ($T \gtrsim 500$ MK) and silicon burning ($T \gtrsim 2.7$ GK). These processes describe the respective connection of the naming elements and the following reaction (see table 2.2). Once these later burning stages start they run through even faster than the previous ones. Silicon burning is also the last nuclear-burning phase in a star. Since it ends in ^{56}Fe , the isotopes are in the most stable configuration and the star can no longer gain energy, due to nuclear reactions. Since the pressure can not be sustained the star collapses in a supernova explosion.

As already mentioned some isotopes can only be produced in the shockwave of these SNe. This is called explosive nucleosynthesis or explosive burning and is primarily characterized by the temperatures reached in the shock region. In these shockwaves temperatures over 5 GK are reached in the interior region of the SNe (up to 3700 km) [Woosley et al., 2002]. The pre-explosive composition leads to a neutron excess from heavy elements disintegrating in the explosion and therefore triggers the r-process. During this rapid neutron-capture process also ^{60}Fe is produced.

^{60}Fe results from the neutron-capture chain $^{58}\text{Fe}(n, \gamma)^{59}\text{Fe}(n, \gamma)^{60}\text{Fe}$ and is destroyed by an additional neutron-capture $^{60}\text{Fe}(n, \gamma)^{61}\text{Fe}$. For the cross-section, $\sigma \approx 23$ mbarn, for the neutron-capture of ^{59}Fe and the short half-life of 44 days, neutron densities of 10^{12} n/cm³ are needed for this production [Lugaro and Chieffi, 2011]. Therefore ^{60}Fe is only produced in the supernova neutron excess of massive star SNe. This is the reason why ^{60}Fe is not ejected through stellar winds and only enters the ISM via SNe.

2.3. Supernovae

Stars with masses $M \geq 8 M_{\odot}$ reach their end in a core-collapse supernova. Stars with masses between $(9 - 100)M_{\odot}$ end in iron-core dissociation, one out of three different mechanisms leading to the implosion of a stellar core. Because only stars with masses $(8 - 9)M_{\odot}$ start the implosion via electron capture and stars with masses $> 100 M_{\odot}$ via

reaction		reaction	
He Burning ($\gtrsim 100$ MK)		O Burning ($\gtrsim 150$ MK)	
$\alpha + \alpha \rightarrow {}^8\text{Be}$	$Q_{\text{tot}} = -0.092 \text{ MeV}$	${}^{16}\text{O} + {}^{16}\text{O} \rightarrow {}^{28}\text{Si} + \alpha$	
${}^8\text{Be} + \alpha \rightarrow {}^{12}\text{C}$	$Q_{\text{tot}} = 7.367 \text{ MeV}$	${}^{16}\text{O} + {}^{16}\text{O} \rightarrow {}^{31}\text{P} + \text{p}$	
Carbon Burning ($\gtrsim 500$ MK)		${}^{16}\text{O} + {}^{16}\text{O} \rightarrow {}^{31}\text{S} + \text{n}$	
${}^{12}\text{C} + {}^{12}\text{C} \rightarrow {}^{20}\text{Ne} + \alpha$		${}^{31}\text{S} \rightarrow {}^{31}\text{P} + \text{e}^+ + \nu$	
${}^{12}\text{C} + {}^{12}\text{C} \rightarrow {}^{23}\text{Na} + \text{p}$		Si Burning ($\gtrsim 2.7$ GK)	
${}^{23}\text{Na} + \text{p} \rightarrow {}^{20}\text{Ne} + \alpha$		${}^{28}\text{Si} + {}^{28}\text{Si} \rightarrow {}^{56}\text{Ni}$	
${}^{23}\text{Na} + \text{p} \rightarrow {}^{24}\text{Mg}$		${}^{28}\text{Si} + (1..7)\alpha \rightarrow {}^{31}\text{S} (\dots {}^{56}\text{Ni})$	
${}^{12}\text{C} + \alpha \rightarrow {}^{16}\text{O}$			
Ne Burning ($\gtrsim 120$ MK)			
${}^{20}\text{Ne} + \gamma \rightarrow {}^{16}\text{O} + \alpha$			
${}^{20}\text{Ne} + \alpha \rightarrow {}^{24}\text{Mg}$			
${}^{24}\text{Mg} + \alpha \rightarrow {}^{28}\text{Si}$			

Table 2.2.: Burning phases in massive stars as shown in [Siegert, 2017]. Processes after He burning only occur in stars with masses over $8 M_{\odot}$, when the necessary temperatures can be reached.

electron-positron pair creation, the iron-core dissociation is the most common. Stars with these masses ($(9 - 100)M_{\odot}$) go through the previously mentioned burning phases until a core consisting entirely of nickel and iron is formed and nuclear burning stops in the core. Above thermal energies of $k_{\text{B}}T \sim 1\text{MeV}$, the iron core becomes unstable due to the gravitational impact, this is where the mass of the core surpasses the Chandrasekhar mass. The core collapses and the iron-core photo-disintegrates. This means photons destroy the iron isotopes into α -particles which then are destroyed into protons and neutrons. The gravitational collapse is accelerated due to electron captures on these protons, with increasing density and temperature forming a so-called runaway because free electrons are removed that held up the pressure due to degeneracy [Woosley et al., 2002]. At a density of $\rho \approx 2.7 \cdot 10^{14} \text{ g cm}^{-3}$ a neutron star is formed and the matter can not be compressed any further. This prompt stop in the collapsing process leads to a “rebound” in the form of a shockwave. The complete destruction of the star results from the shockwave blasting through the different infalling layers above the collapsed core. The shocked matter reaches velocities of $v_{\text{shock}} = (1000 - 10000) \text{ km s}^{-1}$. As mentioned before, in the shock region Nucleosynthesis occurs (explosive burning), and the produced elements are either ejected from the supernova or fall back onto the neutron star depending on the mass cut in this region [Siegert, 2017]. These SNe happen in regions with massive stars, therefore mostly in OB associations. The lifetime of stars depends on their mass, as more massive stars burn faster. Stars with masses $(9 - 100)M_{\odot}$ have a lifespan of $\sim (0.1 - 40) \text{ Myr}$

2.4. Nucleosynthesis Yields

The isotopes that are ejected via SNe or stellar winds are called yields. Since the abundance of different elements depends on the initial stellar mass, the output varies for the masses. In [Limongi and Chieffi, 2018] simulations for massive stars covering the presupernova evolution are conducted, based on a grid between $13 M_{\odot}$ and $120 M_{\odot}$ for metallicities 0, -1, -2, -3 and rotational velocities from $0 - 300 \text{ km s}^{-1}$. Metallicities describe the abundance relation between light elements, hydrogen and helium, and heavier elements, anything of higher order, and therefore has an impact on the composition of a star and the resulting yields. Stars can also rotate around their axis, which also changes the environment and the output of stars. To quantify this property the rotational velocity is used. One assumption that is needed to calibrate the explosion and is used in the simulations in [Limongi and Chieffi, 2018] is that Stars with $25 M_{\odot}$ or higher mass fully collapse into a black hole. This assumption results in a drop in the yields mainly for elements that are produced during explosive burning because they fall back onto the black hole. We calibrate our model later with ^{60}Fe that is produced in explosive burning and therefore only consider stars up to $25 M_{\odot}$ for ^{26}Al and ^{60}Fe yields in the following. For these masses, the yields are also shown in Fig. 2.1 (^{60}Fe) and Fig. 2.2 (^{26}Al).

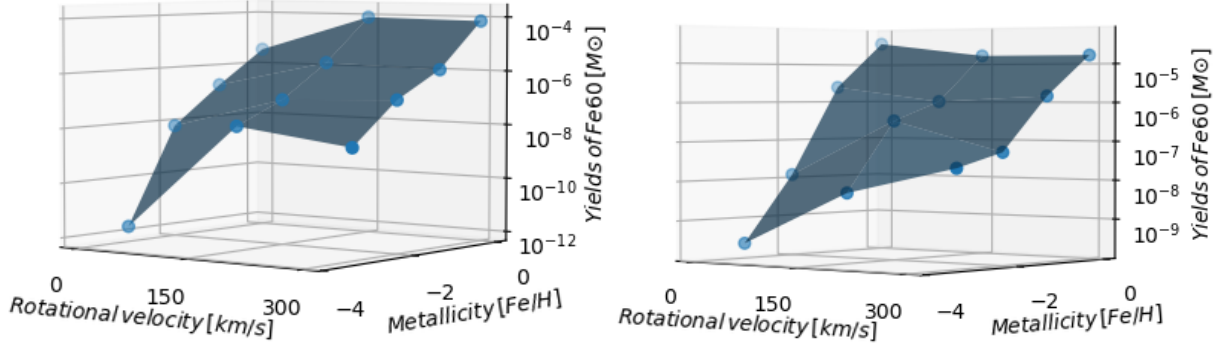


Figure 2.1.: ^{60}Fe yields in dependence on the metallicity and the rotational velocity. The Figure on the left is for a star with a mass of $13 M_{\odot}$ and the right one with a mass of $25 M_{\odot}$. For less massive stars, the dependency on the metallicity and the rotational velocity increases giving a broader range for the yields. The data for the plots is given in [Limongi and Chieffi, 2018].

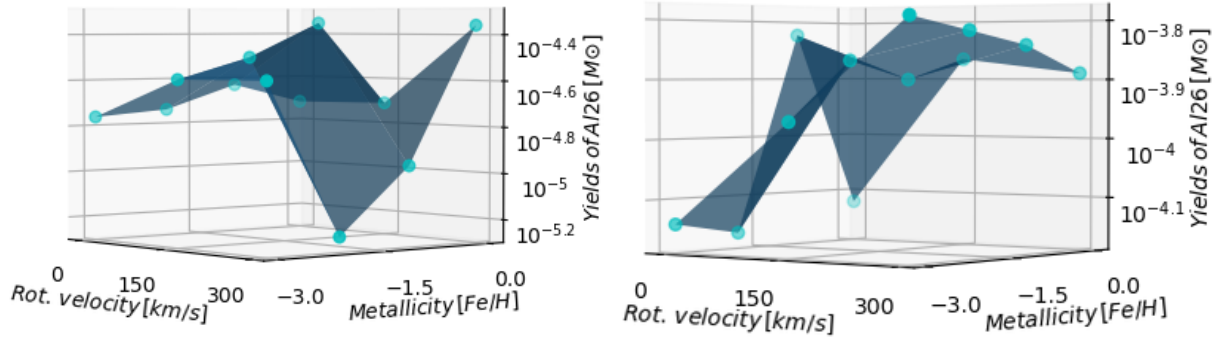


Figure 2.2.: ^{26}Al yields in dependence on the metallicity and the rotational velocity. The Figure on the left is for a star with a mass of $13 M_{\odot}$ and the right one with a mass of $25 M_{\odot}$. For less massive stars, the yields are lower than for the $25 M_{\odot}$ star, while each cover a similar bandwidth in contrast to ^{60}Fe . The data for the plots is given in [Limongi and Chieffi, 2018].

3. Local Bubble

3.1. Introduction to Superbubbles

One feature of the interstellar medium (ISM) in the Milky Way and nearby galaxies are so-called superbubbles. Superbubbles are the result of the cumulative energy output of individual stars in clusters, e.g. stellar winds, ultra-violet radiation, and SNe. This leads to an isotropic effect with the cluster in the center. Superbubbles, which have typically sizes of a few 100 pc, evolve through three phases (see Fig. 3.1). In the first phase, it expands in an adiabatic flow, as the cooling with radiation is too slow to effectively cool the system. In the second phase, a thin shell of interstellar gas emerges from surrounding gas being swept up by the outwards flow. In the third phase, radiative cooling becomes effective slowing down the outer regions of the superbubble [Pleintinger, 2020]. In these superbubbles, the particle density is low with about 10^{-3} cm^{-3} [Krause et al., 2014]. SNe sweeping through the superbubble heat up the inside to temperatures of $\sim 10^6 - 10^7 \text{ K}$ while the shell of atomic (HI or H₂) gas has temperatures of $\sim 100 \text{ K}$ [Pleintinger, 2020]. Idealized, the expansion of the shell is spherical and depends only on the luminosity and the density of the surrounding ISM. The latter is not homogeneous resulting in superbubbles that are not perfect spheres. The compression of gas in the shells can also initiate new star formation [Krause et al., 2014]. The most nearby superbubble is the one surrounding our solar system, the Local Bubble (LB). The Sun entered this structure about 5 Myr ago and is located in the central region of the LB today.

3.2. Morphology of the Local Bubble

The shape of the LB is a consequence of the following factors. On one hand, as for all superbubbles, the expansion is restricted to the surrounding bubbles. On the other hand, how the LB evolved. As it presumably was formed from the energy output from different stars and SNe. The LB is probably born from SNe in the Upper Centaurus Lupus (UCL) and the Lower Centaurus Crux (LCC) about 14 Myr ago. In Fig. 3.2 the position of these star associations is shown in galactic coordinates ([Krause et al., 2018]).

An estimation of 15 SNe could supply the required momentum injection for the expansion velocity of the total shell mass of $1.4 \cdot 10^6 M_{\odot}$ [Zucker et al., 2022]. These factors result in a potato-shaped shell that has many dents and deviations from a sphere, as would be

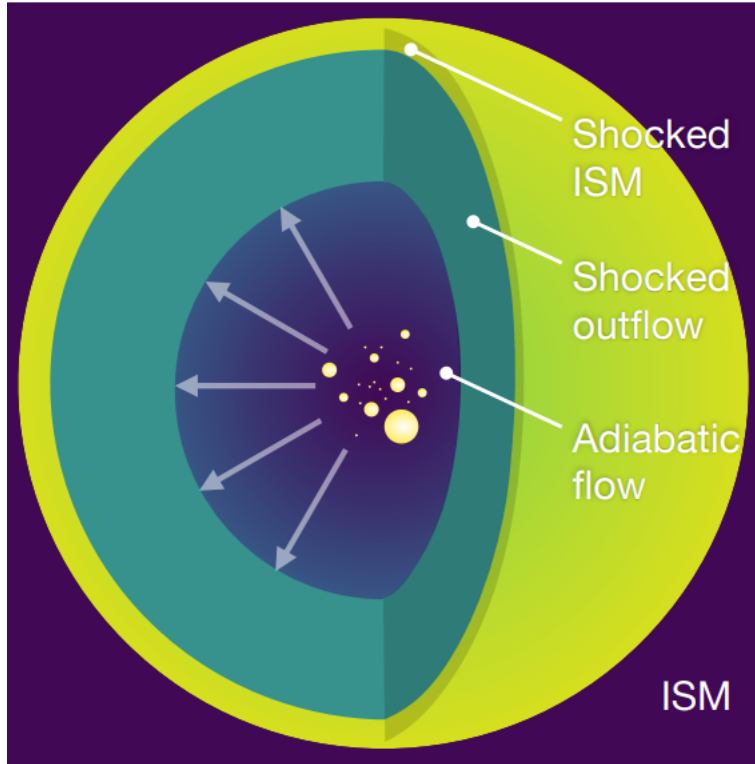


Figure 3.1.: Schematic structure of a superbubble taken from [Pleintinger, 2020]

expected from the density inhomogeneities of the real Galaxy, compared to the scheme (as shown in Sec. 3.1). In Fig. 3.3 the model of Zucker et al. (2022) shows the LB in purple with radii between about 100 pc and 300 pc from the Sun (yellow cross). The green structure in the figure is the neighboring PerTau Bubble, which blocks the expansion of the LB in this direction. The assumption that stars are formed in the compressed gas at the edge of the bubbles is reinforced by the example of the LB. Different star-forming regions such as Taurus, Ophiuchus, Lupus, Chamaeleon, and Corona Australis are associated with the surface of the LB, as well as parts of the Gould Belt [Zucker et al., 2022]. The Gould Belt is a ring of stars in which many OB associations lay. It is inclined to the Galactic Disc at about 20 degrees and has a high star formation rate.

Distance measurements to the enveloping shell were obtained by [Pelgrims, V. et al., 2020]. To fill the space between the measured data spherical harmonic expansion is performed [Pelgrims, V. et al., 2020]. This leads to different smoothness for the whole structure for different orders of spherical harmonics. Starting from a sphere neglecting some deviations from the data up to a heavily deformed construct. We use the parameter i to describe the order of the spherical harmonics used. The value is related to the maximum multipole expansion parameter, l_{max} , which describes the complexity of the structure [Pelgrims, V. et al., 2020]. This interpolation is done in Fig. 3.4 and shown as a cross-cut of the xy-plane for $z = 0$ [Pelgrims, V. et al., 2020]. The data can be exactly met with a high value for i but the structure loses a smooth continuity. The radii resulting for

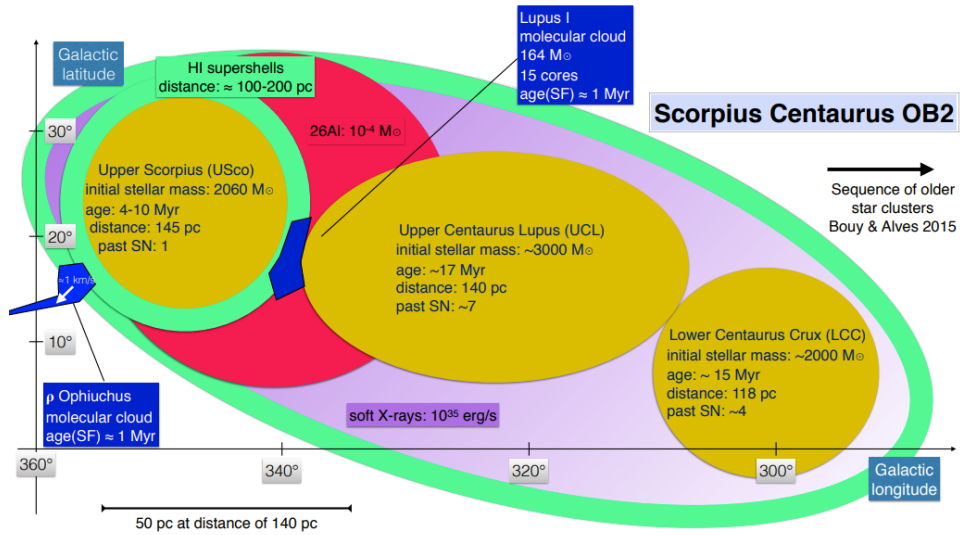


Figure 3.2.: The Scorpius Centaurus region in a summarizing sketch with the observational information. The UCL and the LCC are part of this region. Figure taken from [Krause et al., 2018].

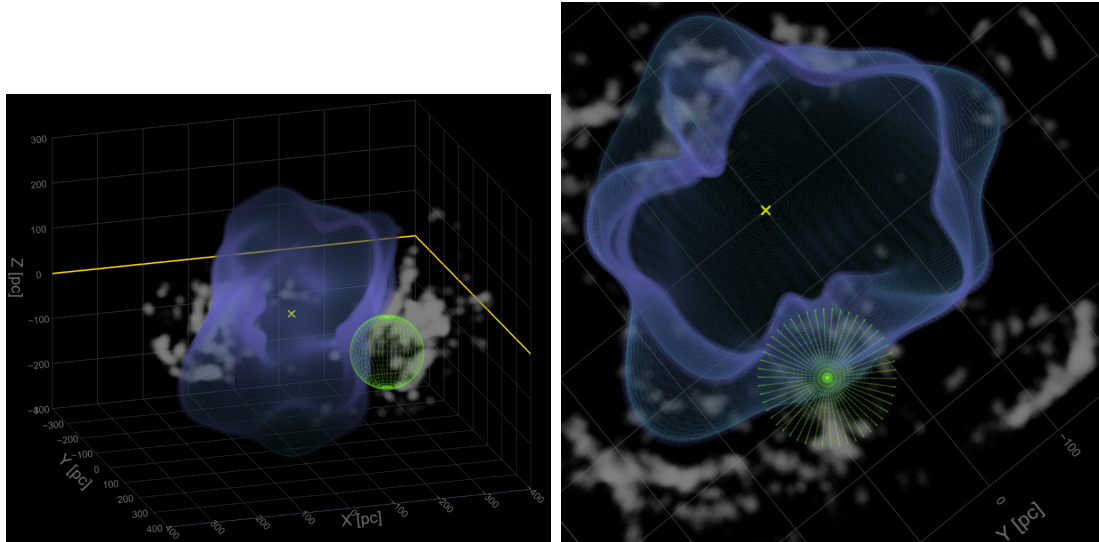


Figure 3.3.: Purple: Local Bubble; green: PerTau Bubble; yellow: Sun; 3D Model of the LB from two viewpoints. The radii from the Sun to the shell reach up to 300 pc. The radii are strongly deformed by adjacent bubbles and the evolution of the LB starting from a sphere. The figure is part of [Zucker et al., 2022] and can also be found here https://faun.rc.fas.harvard.edu/czucker/Paper_Figures/Interactive_Figure1.html.

different i as a whole sky image starting from the Sun is also shown in Fig 3.5. For $i = 1$ the approximation gives a sphere with different distances only due to the fact that the Sun is not exactly in the center of the LB. For the highest order ($i = 8$), the distances seem erratic. Therefore these might not be physical, while the low-order approximation appears to be too simplifying. As a compromise between complexity and anticipation, we use $i = 3$ for our model calculations in Chp. 4. In A the gamma-ray flux whole sky

images for the different i are shown (see Fig. A.6). The total flux changes less than 4% for the different i and therefore we further on only use the one value of $i = 3$.

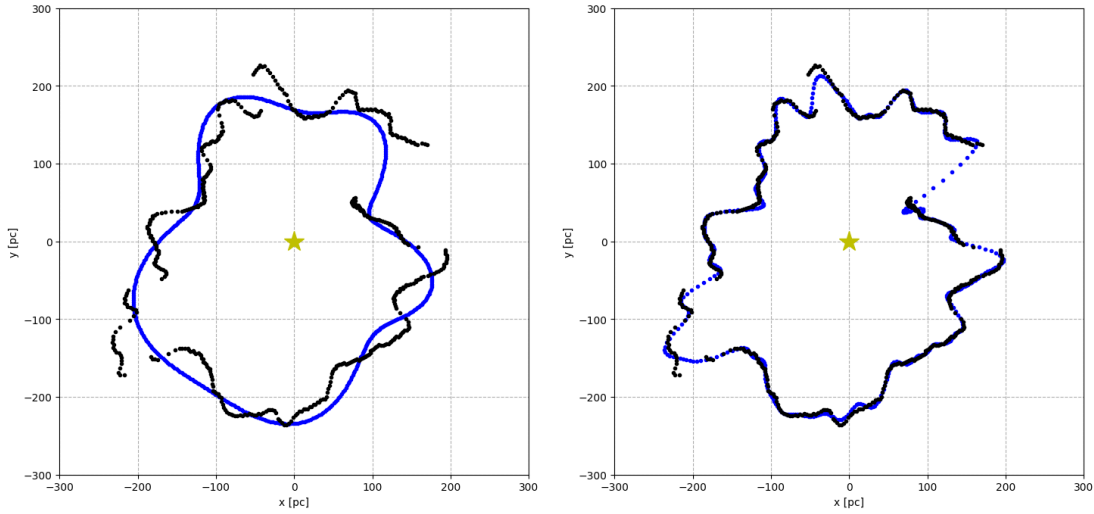


Figure 3.4.: Cross cut of the $z=0$ plane showing the raw data of the dust measurements by [Pelgrims, V. et al., 2020] (black) and two models to interpolate the shape of the LB (blue) for $i = 3$ (left) and $i = 8$ (right). The Sun is in the center of the plane.

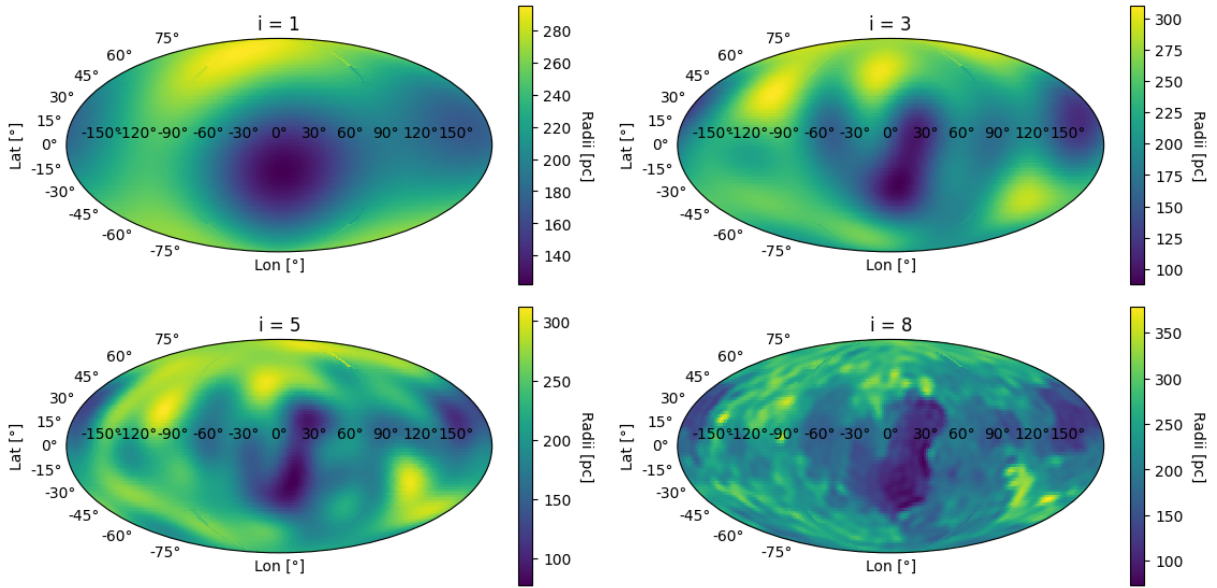


Figure 3.5.: Whole sky image of the radii in pc of the LB from the Sun. The images are the result of different-order spherical harmonics, describing dust extinguishment measurements [Pelgrims, V. et al., 2020]. Here with $i=\{1;3;5;8\}$. For $i = 1$, the structure is almost isotropic and deviates only from equal radii in all directions by the fact that the Sun is not in the center of the Local Bubble, while for $i = 8$ the distances seem erratic resulting in an unsteady structure.

3.3. Pacific Ocean Crust Fe60 Abundance

Given the age of the LB is 14 Myr and the energy input required for the formation had to come from more than 10 SNe (see Sec. 3.2), it can be assumed that the Solar System witnessed one or more SNe since it entered the LB about 5 Myr ago. Indeed ocean crust measurements indicate the deposition of radioactive ^{60}Fe with an extraterrestrial origin [Wallner et al., 2021]. Because ^{60}Fe can not be produced with high abundance in the atmosphere, as a result of cosmic-ray interactions, this measurement has been interpreted as direct evidence for recent (< 10 Myr ago) and nearby (< 100 pc distant) SNe. The abundance of ^{60}Fe on Earth relates a high ^{60}Fe -flux towards Earth with a point in time, as deep layers in the ocean crust relate to earlier epochs. The data from [Wallner et al., 2021] shows two peaks for the ^{60}Fe abundance in the last 8 Myr, which are linked to two SNe in that time [Chaikin et al., 2022]. The ^{60}Fe -yield in core-collapse supernovae is on a scale of $M_{\text{Fe},60} \sim (10^{-6} - 10^{-3})M_{\odot}$. The simulations in [Chaikin et al., 2022] fit the data via the combination of the ^{60}Fe -yield and a new parameter $f_{\text{Fe},60}$, which describes the efficiency of deposition of the isotope on Earth. Using $M_{\text{Fe},60} f_{\text{Fe},60} = 1 \cdot 10^{-7} M_{\odot}$ and $M_{\text{Fe},60} f_{\text{Fe},60} = 0.4 \cdot 10^{-7} M_{\odot}$ for the two SNe, which reached Earth at ≈ 7 Myr and ≈ 3 Myr ago. This is shown in Fig. 3.6 as well as the data from [Wallner et al., 2021]. To match the data the trajectory for the progenitor stars is simulated and time-shifted. The ^{60}Fe is ejected in the SNe with the sound velocity in the ambient region (for superbubbles $v_s = 300 \text{ km s}^{-1}$) in all directions and when it hits the Earth is then deposited on its surface. Another way for ^{60}Fe to reach Earth would be that the Solar System traversed ^{60}Fe enriched clouds [Wallner et al., 2021]. The reason why there is not the same evidence for ^{26}Al deposition on Earth is that ^{26}Al is produced not only in stars but in our own atmosphere, due to cosmic-ray interactions on a bigger scale as ^{60}Fe . This then leads to a higher offset in ^{26}Al deposits and it is inefficient to try finding ^{26}Al that originates from SNe.

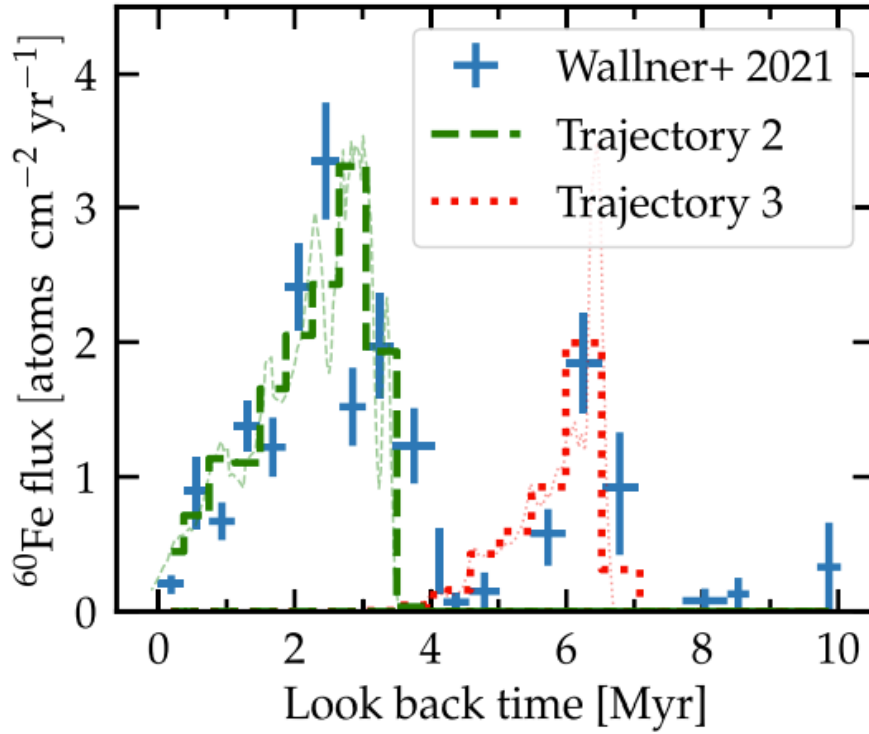


Figure 3.6.: Incorporation of ^{60}Fe as measured by [Wallner et al., 2021]. The two trajectories for the progenitor stars and the resulting SNe are normalized with $M_{\text{Fe},60} f_{\text{Fe},60} = 1 \cdot 10^{-7}$ (green) and $M_{\text{Fe},60} f_{\text{Fe},60} = 0.4 \cdot 10^{-7}$ (red) and shifted in time to fit the data. Figure taken from [Chaikin et al., 2022]

4. Gamma Ray Flux Expectations

In the previous chapter, we concluded that some radioactive deposition happened on Earth 7 and 3 Myr ago. If this deposit is the consequence of core-collapse SNe, we can make predictions for the expected gamma-ray flux from the radioactive ^{60}Fe . Even further we can perform an estimation of how strong the decay gamma rays for ^{26}Al would be. This is possible due to the fact that ^{26}Al is produced in the same sources as ^{60}Fe . To do this we designed a model based on the structure of the LB that uses the total mass of the respective yield and the position inside of the LB for the two SNe.

4.1. Line of Sight inside of the Local Bubble

The first consideration that is used works on the previously introduced LB. We consider that an SN explosion inside this low-density region will fill up the whole construct with the evaluated yields of isotopes. As the isotopes are ejected toward the shell of the LB they also decay resulting in an exponentially declining profile. This is where the line of sight (LOS) comes into play. If we consider our whole sky image, we can cut out a specific solid angle and discuss only the flux coming from this region in the sky. For this we need to integrate over an emissivity, here the gamma-ray emission per unit volume along this ‘line of sight’, we eventually end up with the flux reaching us from this direction out of the whole sky. This looks as follows for our example (Fig. 4.1). The line-of-sight integration begins at the observer. Adding a source of emissivity in the form of two SNe fills the LB with exponentially decaying gamma-ray activity from the location of the SNe away. This is a good enough approximation, considering the sound speed in superbubbles is $c_s = 300 \text{ km s}^{-1}$ and the crossing time for 150 pc (roughly the average distance from a point inside to the shell of the LB) is 0.5 Myr [Krause et al., 2014]. Due to the time scales, we assume that the LB is almost homogeneously filled. This is then in first order an exponentially decaying profile with the radioactive decay times and the sound velocity. The positions that are assumed for the SNe are then weak hotspots in the emissivity profile, while the different radii in different directions have a much larger impact. Integrating the emissivity with an explicit angle to the chosen coordinate system is then the LOS integration for our case. The upper limit for our integral is the shell of the LB. By repeating this integration over a grid of solid angles, which is evenly distributed over longitudes and latitudes we can produce an image of the flux in every pixel. Also,

the dependence of the resulting flux on the position of the SNe is then included in the model.

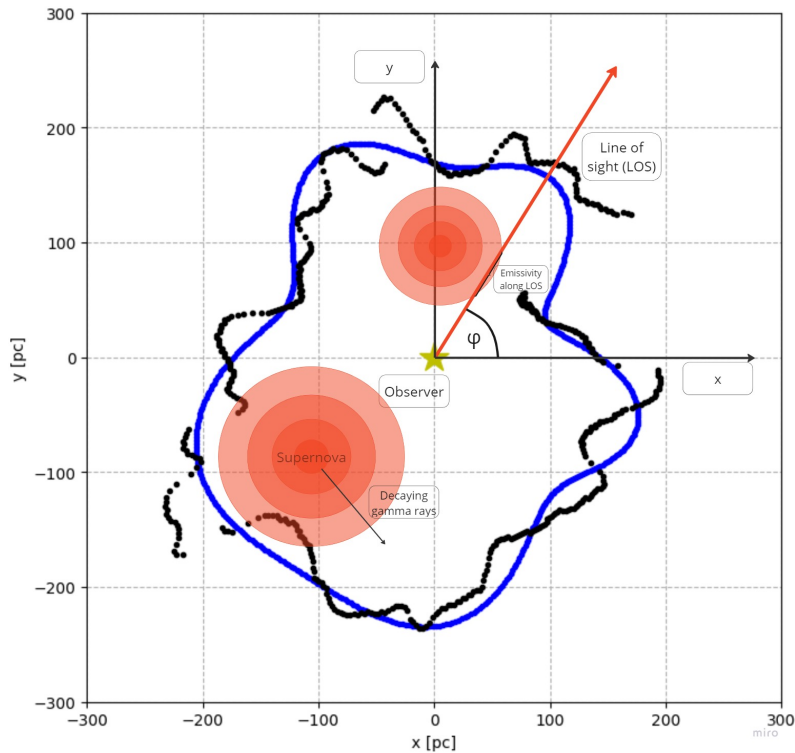


Figure 4.1.: 2D scheme for the LOS integration. Starting from the observer (yellow star) the integration goes along the LOS (red) that is defined for an explicit angle φ . Then, from the center of the SNe away decaying gamma-ray activity, is integrated up to the shell of the LB (blue). This integration yields the gamma-ray flux from this direction in the sky. Repeating this process for a grid of angles over a full sphere results in a whole sky flux image.

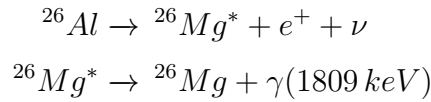
4.2. Gamma-Ray Emission from decaying Isotopes

Now we want to fill the LB with the ‘physics’ for the LOS integration. It is therefore necessary to derive the relation between the mass we put into the model and the emissivity that therefore is produced in the radioactive decay. Thus the activity as a function of time and then as a function of the position in the LB is needed.

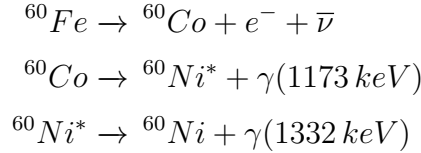
4.2.1. Radioactive decay of Al26 and Fe60

^{26}Al and ^{60}Fe both decay via β -decay. This decay is a process, where a proton (neutron) becomes a neutron (proton) and due to the conservation of charge, a positron (electron) and an electron (anti-) neutrino are released. This gives the two decay chains for these isotopes:

The β^+ -decay of ^{26}Al :



and the β^- -decay of ^{60}Fe :



Even if it is not possible to predict when individual nuclei will decay, a statistical analysis of unstable isotopes provides the half-lives. The half-life $T_{1/2}$ is often given with the decay constant $\lambda = \frac{\ln(2)}{T_{1/2}}$ and is the period in which half of the existing nuclei disintegrate. The decay law reflects that mathematically.

$$\frac{dN(t)}{dt} = -\lambda N(t) \quad (4.1)$$

With the number of particles N and the decay constant λ

The differential equation is solved by

$$N(t) = N_0 \cdot e^{-\lambda t} \quad (4.2)$$

combining (4.1) and (4.2) then gives the activity A and in this case, the luminosity L in units of $[\frac{\text{ph}}{\text{s}}]$.

$$L(t) = A(t) = \lambda \cdot N_0 \cdot e^{-\lambda t} \quad (4.3)$$

The starting number of particles N_0 is the total mass M of the decaying matter divided by the mass of a single particle m . Scaling the luminosity over a spherical shell and using the relation between the time and a constant escape speed of $v_{\text{escape}} = 300 \text{ km s}^{-1}$ gives the flux

$$F(d) = \frac{\lambda \cdot \frac{M}{m} \cdot e^{-\lambda \cdot d/v}}{4\pi d^2} \quad (4.4)$$

Since the gamma rays in these decays are not triggered until a subsequent reaction, one cannot assume a gamma particle with 1809 keV for each decayed ^{26}Al , nor for each decayed ^{60}Fe the two gamma particles with 1173 keV and 1332 keV. In addition, the probability of the β -decay with the respective emission line p is a factor in the equation. We can take the probability for the β -decay also as the probability to get the respective photon since the time scale of the excited isotope to go over in the ground state is much smaller than the characteristic time for the decay. For ^{26}Al the second possibility to be eliminated is

via electron capture that eventually gives the same gamma-ray line of 1809 keV. Therefore all decaying ^{26}Al results in the 1809 keV gamma-ray line

All in all the emissivity along the LOS $\rho(s)$ can be written as the profile $f(s)$ we have times an amplitude ρ_0 with:

$$\begin{aligned}\rho(s) &= \rho_0 \cdot f(s) \\ \rho_0 &= \frac{p \cdot M \cdot \lambda}{m \cdot V} \\ V &= \int d\Omega \int s^2 \cdot f(s) ds\end{aligned}\tag{4.5}$$

with V being a characteristic volume that combines the profile $f(s)$ and the luminosity to get the value for ρ_0 . M is the mass of the whole decaying matter, m is the mass of a single decaying particle, and s is the radial component of the LOS.

Parameter	^{26}Al	^{60}Fe
$\lambda [\text{s}^{-1}]$	$3.07 \cdot 10^{-14}$	$8.39 \cdot 10^{-15}$
p (probability for β -decay)	0.82	0.99
m (particle mass) [u]	25.9797604	59.9198073

Table 4.1.: Isotope parameter for the flux model [Jaeck,].

4.2.2. Numerical Examples

With the information in the previous section, we can perform some numerical estimations. If we use an ejecta mass M_a of isotope $a = \{26, 60\}$, we can estimate the ratio of the respective gamma-ray line luminosities between the 1809 and 1173 keV line, of these decay processes. The 1173 keV is used as a reference for ^{60}Fe since it has the same branching ratio as the 1332 keV. Eq. (4.4) shows that the flux ratios, and therefore the luminosity ratios as well, are merely the inverse ratios of the decay time, τ_a , and atomic mass, m_a , times the exponential decay term. Therefore, given the same age of a radioactive source, the luminosity ratio is:

$$\begin{aligned} \frac{L_{26}}{L_{60}} &= \frac{M_{26}}{M_{60}} \cdot \frac{m_{60}}{m_{26}} \cdot \frac{\tau_{60}}{\tau_{26}} \cdot \exp\left(\frac{\tau_{60}}{\tau_{26}}\right) = \\ &= \frac{M_{26}}{M_{60}} \cdot \frac{60}{26} \cdot \frac{2.6}{0.7} \cdot \exp\left(\frac{2.6}{0.7}\right) = \\ &= \frac{M_{26}}{M_{60}} \cdot 2.3 \cdot 3.7 \cdot 41.0 \approx 350 \frac{M_{26}}{M_{60}}. \end{aligned} \quad (4.6)$$

For yields of the same mass in both isotopes, we get a luminosity of gamma-rays from ^{26}Al that is two orders of magnitudes larger than the same for ^{60}Fe . Getting the same yields is mostly not the case if we review the simulated yields in [Limongi and Chieffi, 2018] that are shown in Fig. 2.1 and Fig. 2.2. The factor of 350 mitigates considering a stellar group instead of an individual star when the ejection time is taken into account. For the example of a group of massive stars, the mass ratio M_{26}/M_{60} may vary between 0.1 and 10 over the lifetime of a massive star (about 20 - 30 Myr). If we consider the temporal evolution of the exponential factor it approaches 1. With this Eq. (4.6) reads:

$$\frac{L_{26}}{L_{60}} \approx 8.5 \frac{M_{26}}{M_{60}} \quad (4.7)$$

And we get a ratio of $\approx 0.85 - 8.5$ for L_{26}/L_{60} of the group of massive star [Pleintinger, 2020]. If we now extend this consideration to an entire galaxy one obtains a mass ratio of $M_{26}/M_{60} = 0.2 - 2.4$ for a luminosity ratio of $M_{26}/M_{60} = 1.7 - 20.4$. Given that ^{26}Al and ^{60}Fe are produced in the same production sites, the luminosity ratio would be the same as the flux ratio we would measure on Earth. The measured value is $18.4 \pm 4.2\%$ for F_{60}/F_{26} which corresponds to the factor of ≈ 5.4 [Wang et al., 2020]. The given values are subject to uncertainties from contributions of the LB, which will be investigated in the following sections.

4.2.3. Constellations for SNe

The next step in deriving the model is the profile that fills up the LB with our emissivity. The profile is the result of the SNe we put inside the LB. Both SNe are then spherical symmetric exponentially decaying functions from their epicenter that overlap. This is then:

$$f(s) = \rho_{0,1}e^{-d_1 \cdot \lambda/v} + \rho_{0,2}e^{-d_2 \cdot \lambda/v}$$

$$\text{with : } d_1 = \sqrt{(x(s) - x_1)^2 + (y(s) - y_1)^2 + (z(s) - z_1)^2} \quad (4.8)$$

$$d_2 = \sqrt{(x(s) - x_2)^2 + (y(s) - y_2)^2 + (z(s) - z_2)^2}$$

With $d_{1/2}$ the distance from the epicenter of the SNe 1/2 to the position on the LOS and s again being the radial component of the LOS e.g. the distance from the observer to the position on the LOS (Fig. 4.2).

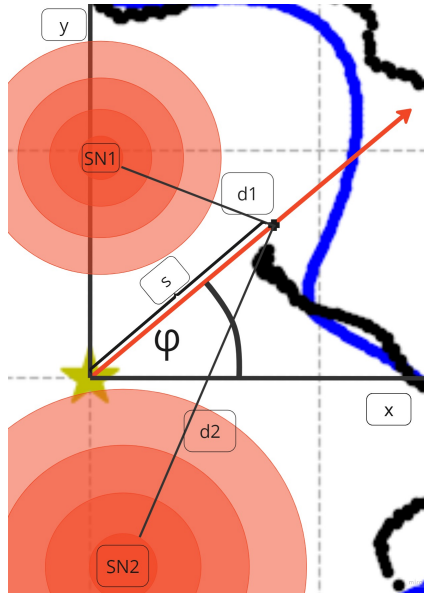


Figure 4.2.: Profile for two SNe. For a particular position on the LOS, the distance to the SNe d is given. The emissivities that decline with the distance d , are added up in the position on the LOS

It is known from the Pacific crust measurements when the SNe yields reached Earth. We, therefore, have to add a time evolution to the emissivity of the form.

$$\rho(t) = \rho(t_0) \cdot e^{-\lambda \cdot \Delta t}$$

$$\Delta t = (t - t_0)$$

Now we can position the SNe at any location in the LB and need to add the time, that the yields needed to reach Earth on top of the age that we get from the Pacific Ocean

crust measurements. This is given for any distance via the escape speed that we assume to be $v_{\text{escape}} = 300 \text{ km s}^{-1}$. It is not possible to make assumptions about the position of the SNe in the LB, because there is no information from where the ^{60}Fe -yields came in the first place. In [Breitschwerdt et al., 2016] simulations for possible explosion sites were performed, but with the same input parameters our model in the end is based on. The mass of the ^{60}Fe yields and the propagation efficiency. We want to keep these properties as free parameters and therefore make our own assumptions. We can narrow down the possibilities to a maximum distance of 100 pc from the SNe to our Solar System. This is a result of a delay between the ^{60}Fe ejecta and the shock front of the explosion, with the ^{60}Fe lagging behind the shockwave [Chaikin et al., 2022].

Now it is possible to put the SNe where we want in the LB, getting the minimum flux for SNe that happened in a distance of 100 pc and the maximum flux for SNe that in a few pc around Solar System. The critical distance for nearby SNe is about 10 pc. The radiation in more nearby SNe would have led to mass extinctions on Earth [Ellis and Schramm, 1995]. Therefore the latter is probably not the case, because devastating natural consequences in this period are not indicated by any evidence. If we combine all the above factors, we obtain the complete model with which we can calculate the flux.

4.3. Calibration of the Supernova-Mass

To calibrate the masses for the model, the relation between a star's mass and the yields in the two isotopes, we want to examine, is used. With the results from the Pacific crust measurements, we search for the total mass of ^{26}Al . To estimate the stellar masses of the two SNe, assumptions about the rotational velocity and metallicity are needed.

4.3.1. Rotational velocity

The rotational velocity forms one of the influences on the stellar composition, as shown in Sect. 2.4. We are interested in massive stars that can produce ^{60}Fe in the first place and explode in core-collapse SNe. Therefore, we examine all stars of spectral classes O and B from the catalog of [Glebocki and Gnacinski, 2005] in terms of rotational velocity under the assumption that the rotational velocities follow a certain distribution. This gives the two respective distributions for the stellar classes (Fig. 4.3). We fit a Gaussian curve plus a linear function to the data to obtain a quantitative statement about the velocity distribution. The function then looks like this:

$$f(x) = A \cdot e^{-\frac{(x-\mu)^2}{2\sigma^2}} + m \cdot x + t \quad (4.9)$$

Uncertainties for the fit parameters are negligible in relation to the resulting variances for the expected values. This gives the following fit parameters:

Parameter	O-stars	B-stars
A (Amplitude)	52.14	348.43
μ (Gaussian peak)	104.34	-53.88
σ (Gaussian width)	33.92	194.90
m (Linear slope)	-0.0073	not accounted for
t (Linear offset)	7.15	not accounted for

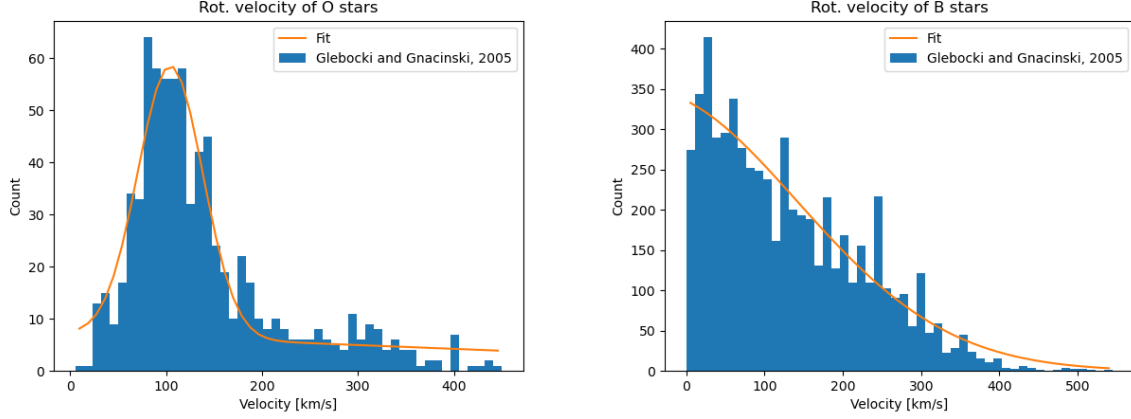


Figure 4.3.: Rotational velocities of stars in the [Glebocki and Gnacinski, 2005]-catalog. The orange line is the combination of a Gaussian curve and a linear function fitted to the data. While O stars hardly occur without rotational velocities, the frequency of B stars decreases steadily with higher rotational velocities.

To get the expected value of the rotational velocities $\langle v \rangle$ for O and B-stars and the respective variance σ^2 the following equations are used.

$$\langle v \rangle = \frac{\int_0^{v_{max}} v \cdot f(v) dv}{\int_0^{v_{max}} f(v) dv} \quad (4.10)$$

$$\sigma^2 = \frac{\int_0^{v_{max}} (v - \langle v \rangle)^2 \cdot f(v) dv}{\int_0^{v_{max}} f(v) dv} \quad (4.11)$$

The resulting rotational velocities are then $v_O = (140 \pm 90) \text{ km s}^{-1}$ for O-stars and $v_B = (135 \pm 104) \text{ km s}^{-1}$ for stars of spectral class B. The band forming the rotational velocities of the B stars with up to one standard deviation also includes the full band concerning the O stars. Since in our case, neither preference for O stars nor B stars is present, the larger band of the B stars is used in the following. The velocity band then reads:

$$V_{\text{rot-exp}} = (30 - 240) \text{ km s}^{-1}$$

4.3.2. Metallicity

Another classification parameter for stars is the so-called metallicity. In astrophysics, all elements that are heavier than hydrogen and helium are called ‘metals’ therefore the abundance of high-order nuclei can be represented as a relative value between two elements. One of these metals (here iron) and one out of hydrogen or helium (here hydrogen). As shown in section 2.4 the yields of elements are also linked to the metallicity in a star, as both properties represent the abundance of isotopes. The logarithmic scale in which we define metallicity is:

$$[\text{Fe}/\text{H}] = \log_{10} \frac{([\text{Fe}/\text{H}]_{\text{star}})}{([\text{Fe}/\text{H}]_{\odot})} \quad (4.12)$$

One way to estimate the metallicity of stars in the solar vicinity is via the metallicity gradient in the MW. From [Cheng et al., 2012] the metallicity for small distances to the Galactic Disc z (minimum in this paper $0.15 \text{ kpc} < |z| < 0.25 \text{ kpc}$) is known and illustrated concerning the galactocentric radius in Fig. 4.4. Additionally, also the uncertainties for the slope are given resulting in a maximum, best, and minimum linear regression in metallicities. To estimate in solar vicinity the distance from the Sun to the galactic center is needed, which is $R_{\odot} = (8178 \pm 13_{\text{stat.}} \pm 22_{\text{syst.}}) \text{ pc}$ [GRAVITY Collaboration et al., 2019]. The first uncertainty is statistical while the second one is systematic. In combination with an average distance to the Galactic Disc in our range of $\langle |z| \rangle = 0.2 \text{ kpc}$ this provides a galactocentric radius of $R = 8.176 \text{ kpc}$, with the radius being the projection on to the Galactic Disc. For this radius the different functions yield the three metallicities of $(\text{Fe}/\text{H})_{\text{min}} = -0.899$, $(\text{Fe}/\text{H})_{\text{best}} = -0.540$, and $(\text{Fe}/\text{H})_{\text{max}} = -0.294$. Therefore we get a metallicity band of:

$$-([\text{Fe}/\text{H}]_{\text{exp}}) = (0.294 - 0.899)$$

Considering the age of the LB it is fair to assume that the stars that we examine were way younger than the stars that are described by this metallicity gradient which are closer to the Sun’s age. Therefore in the following, in addition to the found band, we also evaluate a higher value in metallicity, since younger stars usually form in metallicity enhanced regions. So we also use the estimated metallicity of

$$([\text{Fe}/\text{H}]_{\text{supersolar}}) = 0.50$$

later in a supplementary evaluation, where we also extrapolate the stellar evolution yields from [Limongi and Chieffi, 2018] because they only calculated them up to solar metallicities. Therefore we use the metallicity gradient in the following.

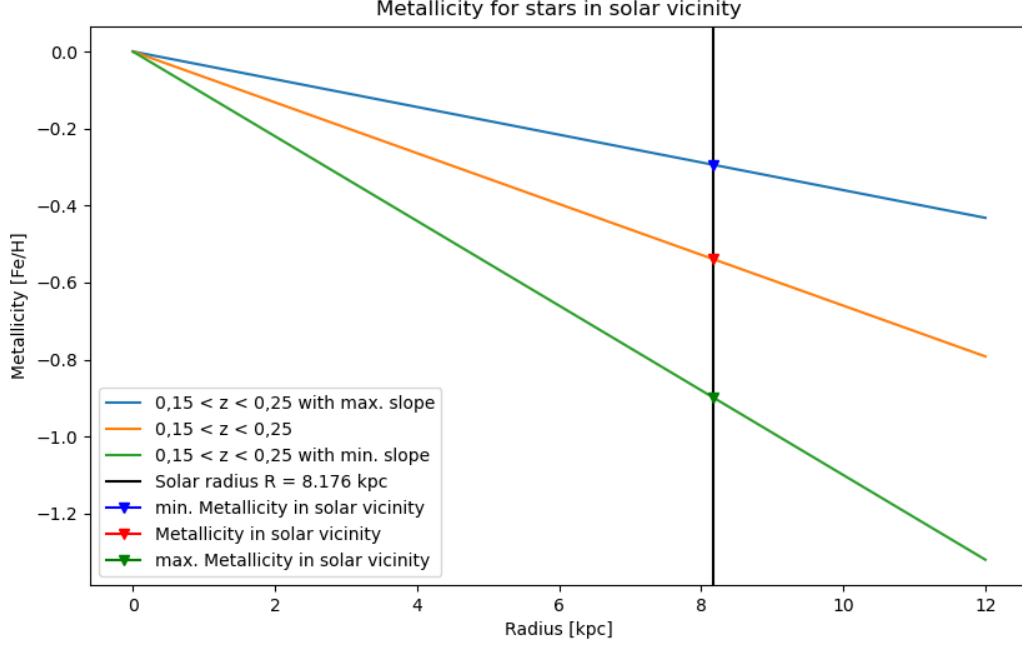


Figure 4.4.: Metallicity of stars at a distance to the Galactic plane of $0.15 \text{ kpc} < |Z| < 0.25 \text{ kpc}$ with the results of [Cheng et al., 2012]. The three different slopes are the result of the best value and its uncertainties in both directions. To obtain values for our solar vicinity we use a radius to the galactic center of $R_{\odot} = (8178 \pm 13_{\text{stat.}} \pm 22_{\text{syst.}}) \text{ pc}$ [GRAVITY Collaboration et al., 2019]. With height of $\langle Z \rangle = 0.2 \text{ kpc}$ we get a Radius of $R = 8.176 \text{ kpc}$. This results in metallicities between $[\text{Fe}/\text{H}] = ((-0.899) - (-0.294))$.

4.3.3. Estimated Aluminum 26 Yields

With the results for the rotational velocity and the metallicity, it is now possible to create a 2D grid with the respective bands in rotational velocities and metallicities. This grid then is used as an area in which we can interpolate between the data for the yields in Sec. 2.4. This process is done for the ^{60}Fe and the ^{26}Al yields, in each mass ($M = \{13; 15; 20; 25\} M_{\odot}$) see Fig. A.2. Before putting together all the pieces, it is necessary to assume a value for the propagation/efficiency parameter $f_{\text{Fe},60}$ that is already introduced in Sect. 3.3.

Since the fraction of dust extinction alone is on the order of ~ 0.01 [Chaikin et al., 2022], we take this value as the maximum propagation/minimum value for $f_{\text{Fe},60}$. Also, the uptake can reduce the actual abundance of ^{60}Fe to be found. Therefore, we assume a less effective propagation and distribution with a value of $f_{\text{Fe},60} = 0.05$. The interpolation provides a minimum and a maximum yield for all these masses. Plotting this gives a band of possible yields concerning the mass of the star in addition to the ^{60}Fe total masses for the two SNe, considering the two $f_{\text{Fe},60}$, Fig. 4.5. For the maximum distribution with $f_{\text{Fe},60} = 0.01$, the specific SN yields in ^{60}Fe can be produced in all the star masses in the

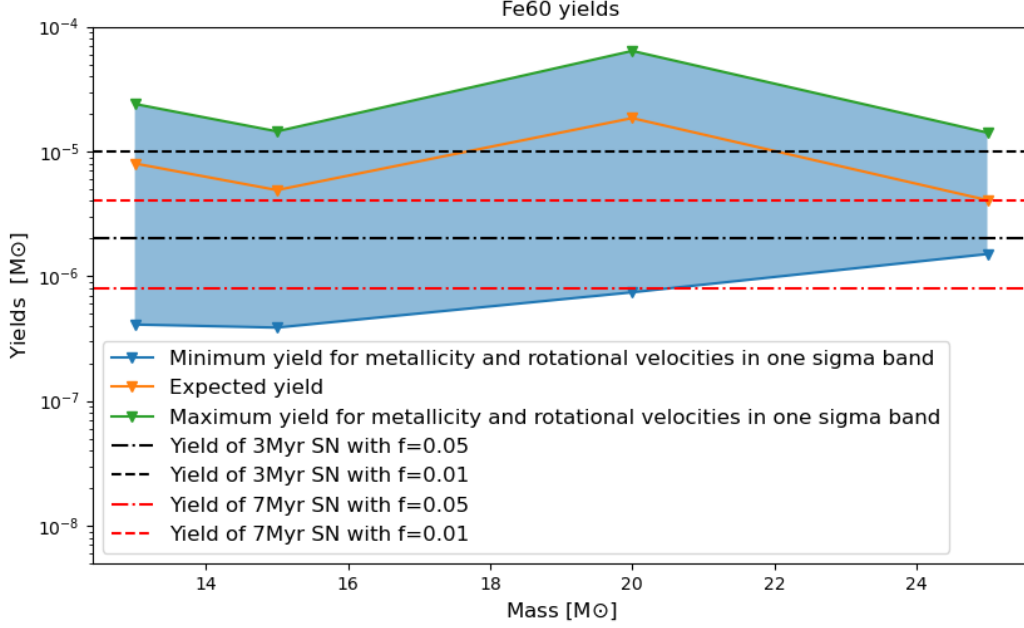


Figure 4.5.: With interpolation in the [Limongi and Chieffi, 2018] values expected ^{60}Fe yields that stars from masses between $13 M_{\odot}$ and $25 M_{\odot}$ produce for the mean values in rotational velocity and metallicity (orange). Additional band with interpolated yields in $1\text{-}\sigma$ rotational velocity deviations and $1\text{-}\sigma$ metallicity deviations (blue shaded). The yields for the SNe, as a result of the Pacific crust measurements, are given for two propagation values $f_{\text{Fe},60} = 0.05/0.01$ (the 7 Myr old SN (red) and the 3 Myr old SN (black)). For $f_{\text{Fe},60} = 0.05$ there is a cutoff at $M_{\text{max}} = 20.5 M_{\odot}$ for the 7 Myr old SN.

given range. This is different for a higher $f_{\text{Fe},60}$, here a cutoff for the 7 Myr old supernova with $M_{\text{max}} = 20.5 M_{\odot}$ maximum stellar mass is shown.

Using the same grid and method for ^{26}Al results in a similar Figure than for ^{60}Fe (Fig. 4.6). As we conclude from the display of the Iron the two SNe originated from stars with the masses:

$$M_{7\text{Myr}} = (13.00 - 20.53) M_{\odot}$$

$$M_{3\text{Myr}} = (13.00 - 25.00) M_{\odot}$$

Herewith we get values for the total mass of Aluminum that could have been ejected in these SNe and their respective iron yields:

$$M_{\text{Al } 7\text{Myr}} = (2.06 - 9.63) \cdot 10^{-5} M_{\odot}$$

$$M_{\text{Al } 3\text{Myr}} = (2.06 - 13.7) \cdot 10^{-5} M_{\odot}$$

$$M_{\text{Fe } 7\text{Myr}} = 0.20 \cdot 10^{-5} M_{\odot}$$

$$M_{\text{Fe } 3\text{Myr}} = 0.08 \cdot 10^{-5} M_{\odot}$$

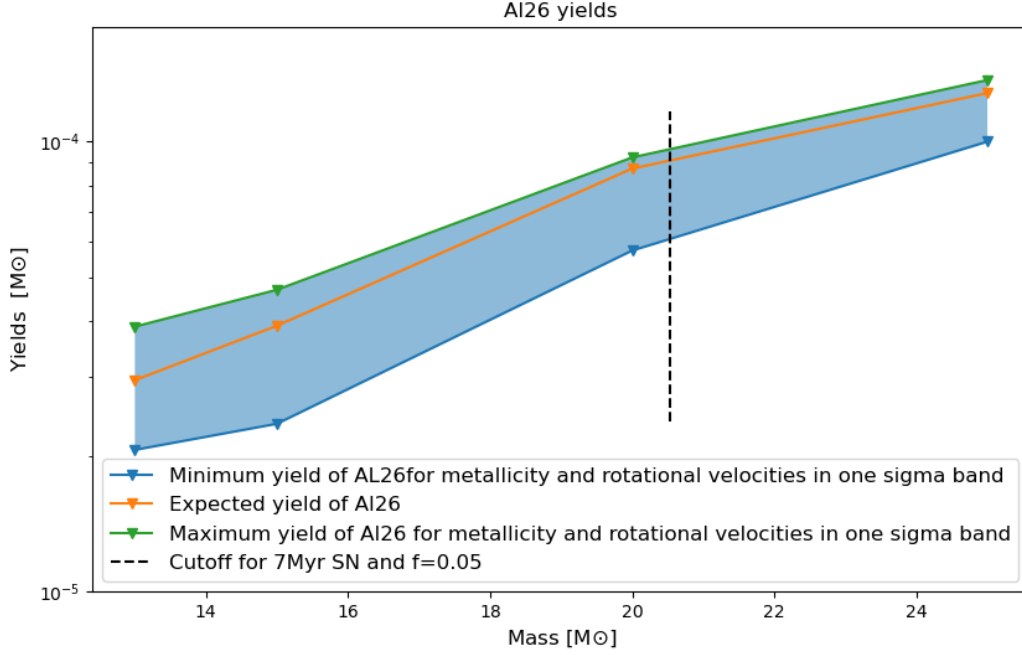


Figure 4.6.: With interpolation in the [Limongi and Chieffi, 2018] values expected ^{26}Al yields that stars from masses between $13 M_{\odot}$ and $25 M_{\odot}$ produce for the mean values in rotational velocity and metallicity (orange). Additional band with interpolated yields in $1\text{-}\sigma$ rotational velocity deviations and $1\text{-}\sigma$ metallicity deviations (blue shaded). The cutoff for the 7Myr old SN with $f_{\text{Fe},60} = 0.05$ is at $M_{\text{max}} = 20.5 M_{\odot}$

4.3.4. Extrapolation to supersolar Metallicities

As already mentioned in Sec. 4.3.2 there is an alternative approach assuming the metallicity in the progenitor stars. Here we use the relation between the metallicity and the period in which stars are born. The metallicity increases for younger stars because the gas over a star's lifetime cycle is enriched with the in these stars produced metals. Therefore we assume for the SNe, resulting from young stars, a metallicity of $([\text{Fe}/\text{H}]_{\text{supersolar}} = 0.5)$. We have to extrapolate values for this high metallicity to use the same method as for the interpolated data in the [Limongi and Chieffi, 2018] grid of yields. Therefore we use the interpolated data for the $1\text{-}\sigma$ band of rotational velocities and the two highest metallicities in the grid (Fig. A.3) as starting points for a linear extrapolation. This linear relation is shown for the mass of $M = 13 M_{\odot}$ in Fig. 4.7 and results in a maximum and a minimum yield for the masses between $13 M_{\odot}$ and $25 M_{\odot}$. Now the same method as before is used and the yields for the masses in their maximum and minimum deviations then give Fig. 4.8. The extrapolated yields for ^{60}Fe are significantly higher than the previously interpolated values for lower metallicities. To match the data for the Pacific crust Iron abundance on Earth with the now emerged band of yields, we have to assume a very poor

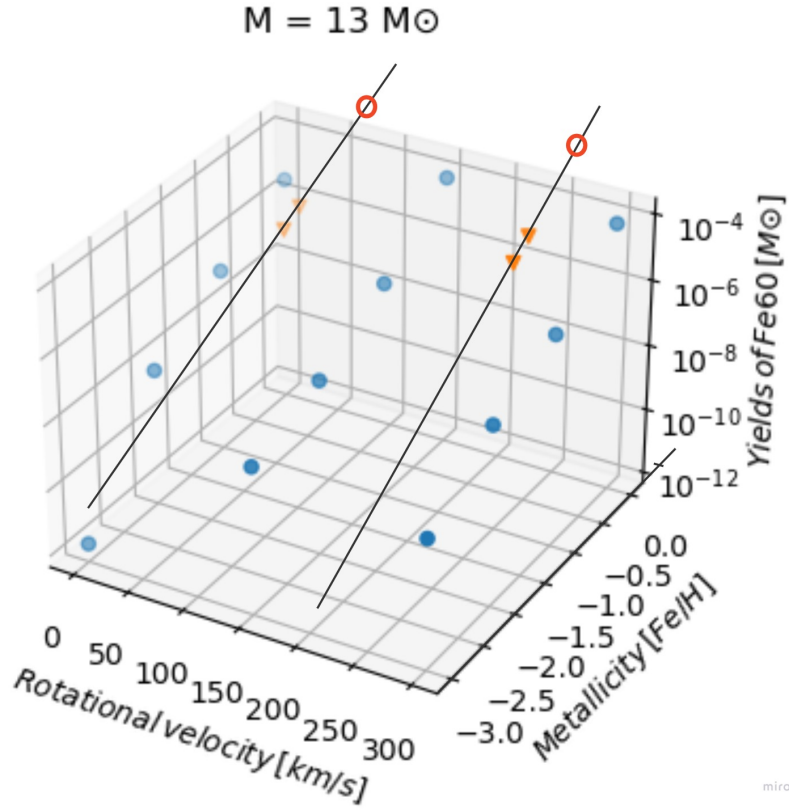


Figure 4.7.: Schematic linear extrapolation of two yields for two points each. Progenitor star mass is $M = 13 M_{\odot}$. For the metallicity of ($[Fe/H] = 0.5$) the extrapolated yields (red circles) are $M_{\text{extra}} = 0.749 \cdot 10^{-5} M_{\odot}$ and $M_{\text{extra}} = 7.15 \cdot 10^{-5} M_{\odot}$.

distribution on Earth. This results in a small propagation/efficiency parameter $f_{\text{Fe},60}$. Two possibilities here are $f_{\text{Fe},60} = 4.0 \cdot 10^{-3}$ and $f_{\text{Fe},60} = 2.0 \cdot 10^{-3}$. Both these values describe higher yields of ^{60}Fe than for the low metallicities, but the same abundance on Earth.

For $f_{\text{Fe},60} = 2.0 \cdot 10^{-3}$ this gives:

$$M_{7Myr} = (13.0 - 25) M_{\odot}$$

$$M_{3Myr} = ((13.0 - 13.7) \& (16.8 - 24.0)) M_{\odot}$$

And for $f_{\text{Fe},60} = 4.0 \cdot 10^{-3}$:

$$M_{7Myr} = (13.0 - 16.5) M_{\odot}$$

$$M_{3Myr} = ((13.0 - 25.0)) M_{\odot}$$

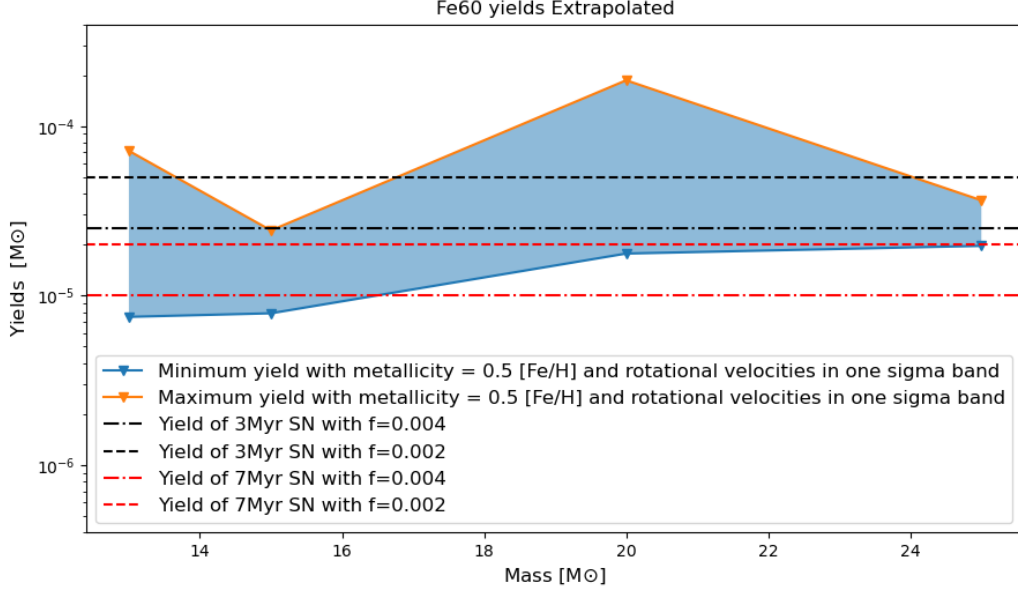


Figure 4.8.: To the [Limongi and Chieffi, 2018] values extrapolated ^{60}Fe yields that stars from masses between $13M_{\odot}$ and $25M_{\odot}$ produce with a metallicity of $[\text{Fe}/\text{H}] = 0.5$. The band results for $1-\sigma$ rotational velocity deviations (blue shaded). The yields for the SNe, as a result of the Pacific Crust measurements, are given for two propagation values $f_{\text{Fe},60} = 0.005/0.002$ (the 7Myr old SN (red) and the 3Myr old SN (black)).

If we now extrapolate the ^{26}Al yields in the same way and add the evaluated ranges for the stars' masses (Fig. 4.9) we get the possible yields that SNe with the given conditions could produce.: For $f_{\text{Fe},60} = 2.0 \cdot 10^{-3}$:

$$M_{\text{Al } 7\text{Myr}} = (1.55 - 13.0) \cdot 10^{-5} M_{\odot}$$

$$M_{\text{Al } 3\text{Myr}} = (1.55 - 11.4) \cdot 10^{-5} M_{\odot}$$

$$M_{\text{Fe } 7\text{Myr}} = 5.00 \cdot 10^{-5} M_{\odot}$$

$$M_{\text{Fe } 3\text{Myr}} = 2.00 \cdot 10^{-5} M_{\odot}$$

And for $f_{\text{Fe},60} = 4.0 \cdot 10^{-3}$:

$$M_{^{26}\text{Al } 7\text{Myr}} = (1.55 - 5.94)10^{-5} M_{\odot}$$

$$M_{^{26}\text{Al } 3\text{Myr}} = (1.55 - 13.0)10^{-5} M_{\odot}$$

$$M_{^{60}\text{Fe } 7\text{Myr}} = 2.50 \cdot 10^{-5} M_{\odot}$$

$$M_{^{60}\text{Fe } 3\text{Myr}} = 1.00 \cdot 10^{-5} M_{\odot}$$

The ^{60}Fe yields increase much more than the ^{26}Al yields for higher metallicities. The increase is purely logical given how the metallicity is defined as the relation between the iron and hydrogen abundances. For the ^{26}Al , the dependence on metallicity is less strong.

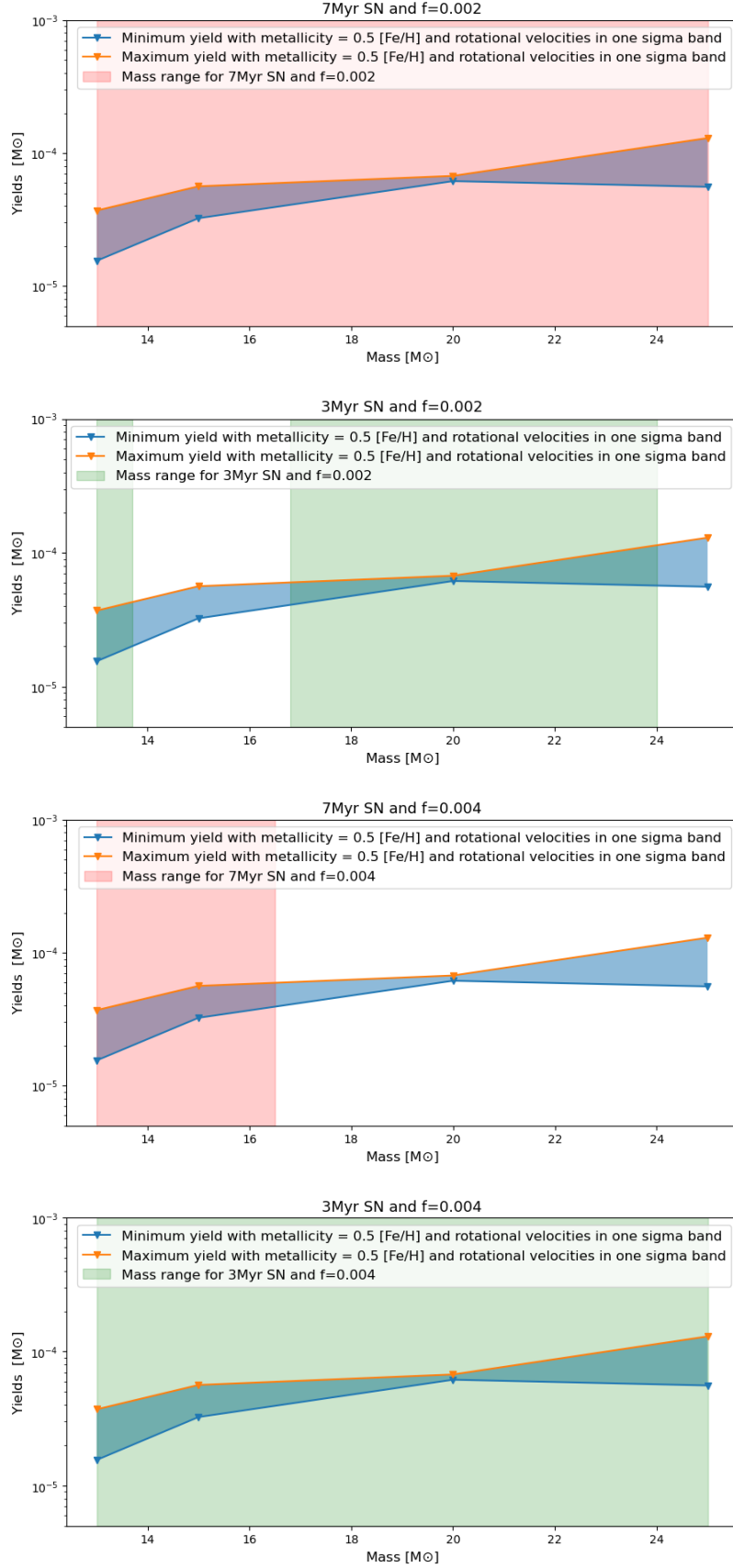


Figure 4.9.: ^{26}Al extrapolated yields that stars from masses between $13M_{\odot}$ and $25M_{\odot}$ produce with a metallicity of $(\text{Fe}/\text{H}) = 0.5$. The Band results for $1\text{-}\sigma$ rotational velocity deviations (blue shaded). For two propagation values $f_{\text{Fe},60} = 0.005/0.002$ and the two SNe each, the star's mass ranges are added, as they are possible with the ^{60}Fe yields.

Yields		
for $-[\text{Fe}/\text{H}] = (0.294 - 0.899)$		
	^{26}Al	^{60}Fe
7 Myr	$(2.06 - 9.63) \cdot 10^{-5} M_{\odot}$	$0.20 \cdot 10^{-5} M_{\odot}$
3 Myr	$(2.06 - 13.7) \cdot 10^{-5} M_{\odot}$	$0.08 \cdot 10^{-5} M_{\odot}$
for $[\text{Fe}/\text{H}] = 0.5$ (supersolar)		
with $f_{\text{Fe},60} = 0.002$		
	^{26}Al	^{60}Fe
7 Myr	$(1.55 - 13.0) \cdot 10^{-5} M_{\odot}$	$5.00 \cdot 10^{-5} M_{\odot}$
3 Myr	$(1.55 - 11.4) \cdot 10^{-5} M_{\odot}$	$2.00 \cdot 10^{-5} M_{\odot}$
with $f_{\text{Fe},60} = 0.004$		
	^{26}Al	^{60}Fe
7 Myr	$(1.55 - 5.94) \cdot 10^{-5} M_{\odot}$	$2.50 \cdot 10^{-5} M_{\odot}$
3 Myr	$(1.55 - 13.0) \cdot 10^{-5} M_{\odot}$	$1.00 \cdot 10^{-5} M_{\odot}$

Table 4.2.: Possible yields for different configurations resulting from the two approaches in metallicity, being the metallicity gradient in the MW and supersolar metallicities for young stars.

This is because the production of ^{26}Al starts earlier in stars and does not require many heavy elements as seed material. The resulting yields so far are also shown in Tab. 4.2

4.4. Expected Gamma-Ray All-Sky Images

From the considerations in the sections above, the model expectations for the gamma-ray flux of the entire sky will now be calculated. For this, we use the following assumptions and test different configurations. The different cases are the combination of the possible different yields for the two isotopes with the two metallicities and different positions of the SNe in the LB. This gives the constellations that are shown in Tab. 4.3.

The gamma-ray flux maps that we get for the different constellations (see Tab. 4.3) all show the structure of the LB if compared to the different radii in Sec. 3.2. Here we see the hotspots for parts of the sky where the LB is further extended. Also, the flux is aligned with the Galactic plane along zero latitude, this makes sense as the LB is a ‘more’ bubble-like structure in the plane and might open up in chimney-like structures for higher latitudes, leading to an outflow for high latitudes. In contrast to the Galaxy, the LB flux values do not cut off for these higher latitudes, this could help to possibly detect the LB gamma-ray flux in the future Sec.5. Also, the UCL and the LCC appear relatively weak in the flux maps (projected in the maps with the positions in Fig. 3.2) while we see a strong emission for a longitude of -90. It is noted, that for our maps, we use a bin size of $3^{\circ} \times 3^{\circ}$ and plot the flux per steradian in the pixels. Also all maps regarding the ^{60}Fe can be found in Chp. A.

Constellation Nr.	7 Myr ago	3 Myr ago	Total flux [ph cm ⁻² s ⁻¹]	Isotope
1	$9.63 \cdot 10^{-5} M_{\odot}$	$13.7 \cdot 10^{-5} M_{\odot}$	$6.4 \cdot 10^{-6}$	²⁶ Al
SNe position	(0; 0; 0)	(0; 0; 0)		
2	$5.0 \cdot 10^{-5}$	$7.5 \cdot 10^{-5}$	$3.5 \cdot 10^{-6}$	²⁶ Al
SNe position	(0; 0; 0)	(0; 0; 0)		
3	$1.55 \cdot 10^{-5}$	$1.55 \cdot 10^{-5}$	$7.3 \cdot 10^{-7}$	²⁶ Al
SNe position	(0; 0; 0)	(0; 0; 0)		(Fig. 4.10)
4	$5.0 \cdot 10^{-5}$	$2.0 \cdot 10^{-5}$	$2.2 \cdot 10^{-6}$	⁶⁰ Fe
SNe position	(0; 0; 0)	(0; 0; 0)		
5	$2.5 \cdot 10^{-5}$	$1.0 \cdot 10^{-5}$	$1.1 \cdot 10^{-6}$	⁶⁰ Fe
SNe position	(0; 0; 0)	(0; 0; 0)		
6	$0.20 \cdot 10^{-5}$	$0.08 \cdot 10^{-5}$	$5.0 \cdot 10^{-8}$	⁶⁰ Fe
SNe position	(0; 0; 0)	(0; 0; 0)		(Fig. A.4)
7	$5.0 \cdot 10^{-5}$	$7.5 \cdot 10^{-5}$	$2.3 \cdot 10^{-6}$	²⁶ Al
SNe position	(0; 100; 0)	(0; -100; 0)		
8	$5.0 \cdot 10^{-5}$	$7.5 \cdot 10^{-5}$	$2.3 \cdot 10^{-6}$	²⁶ Al
SNe position	(0; 100; 0)	(0; 100; 0)		
9	$5.0 \cdot 10^{-5}$	$7.5 \cdot 10^{-5}$	$2.3 \cdot 10^{-6}$	²⁶ Al
SNe position	(0; 100; 0)	(0; 0; 100)		(Fig. 4.11)
10	$2.5 \cdot 10^{-5}$	$1.0 \cdot 10^{-5}$	$4.5 \cdot 10^{-8}$	⁶⁰ Fe
SNe position	(0; 100; 0)	(0; -100; 0)		
11	$2.5 \cdot 10^{-5}$	$1.0 \cdot 10^{-5}$	$4.5 \cdot 10^{-8}$	⁶⁰ Fe
SNe position	(0; 100; 0)	(0; 100; 0)		
12	$2.5 \cdot 10^{-5}$	$1.0 \cdot 10^{-5}$	$4.5 \cdot 10^{-8}$	⁶⁰ Fe
SNe position	(0; 100; 0)	(0; 0; 100)		(Fig. A.5)

Table 4.3.: The different constellations for our two SNe with age 7 and 3 Myr. We take the yields in one isotope and give it a position inside of the LB. The resulting whole sky images can be found below (linked under the isotope). The positions of the SNe are given in Cartesian coordinates.

For the different constellations, two effects show up. If we change the position of the SNe the total gamma-ray flux does not (or only in the slightest see Sec. 4.4) change but we get different regions of the LB highlighted (see Fig 4.11). If we change the input for the masses of the isotopes we get the same structural image but with different total gamma-ray fluxes (see Fig. 4.10).

Total Flux

The total flux we obtain for the different constellations only changes significantly with the input yields. For the different positions in the LB but with the same distance to the observer, we obtain the same fluxes within e.g. 98.3% for constellations 7 & 8. The deviations are then only a result of the difference in the shape of the LB around the two positions. For the different possible yields, that we estimated above, we get for ²⁶Al (with the SNe in the center) total gamma-ray flux in between $F_{1809\text{keV}} = (0.73 - 6.4) \cdot 10^{-6} \text{ph cm}^{-2} \text{s}^{-1}$ and for

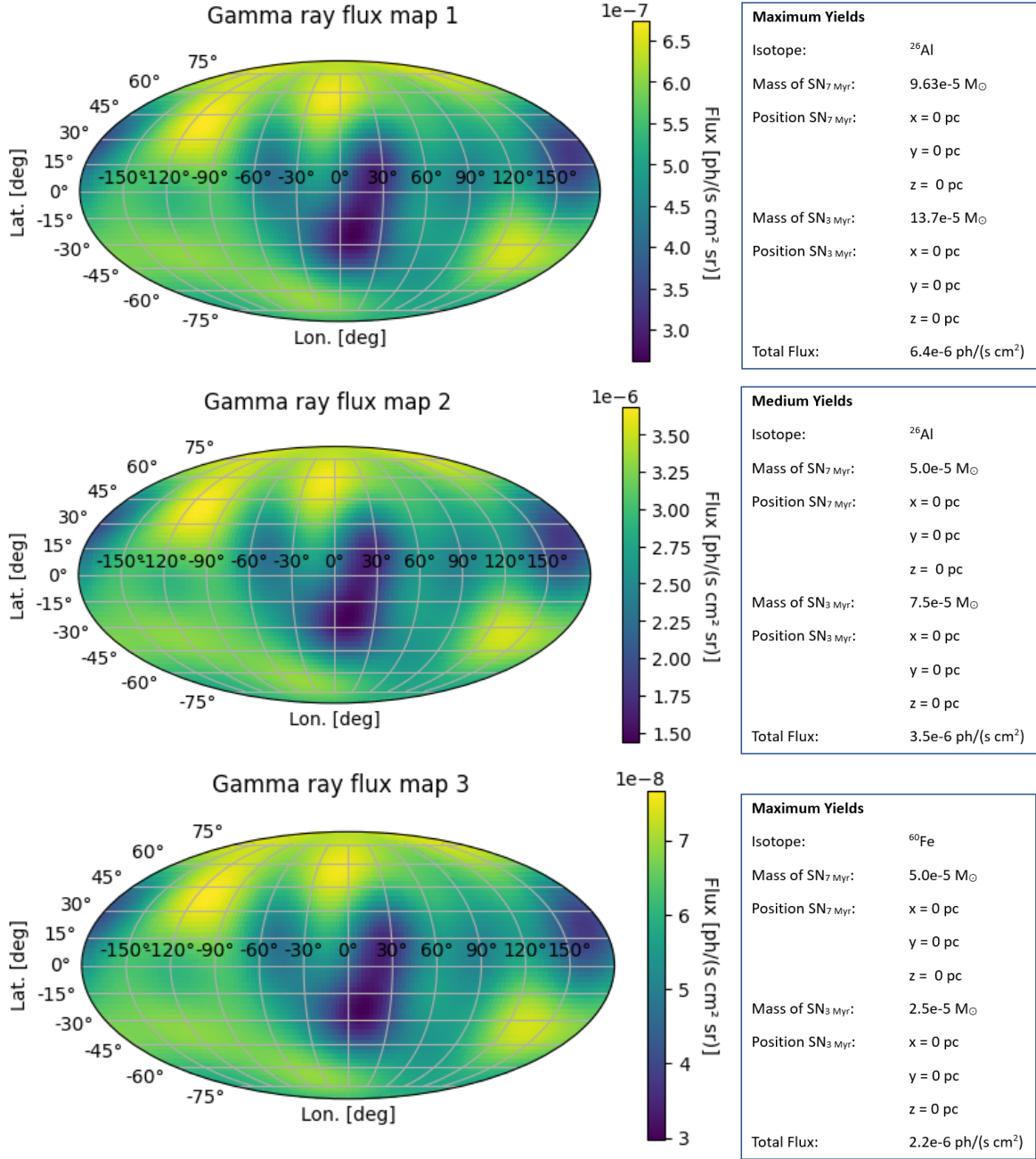


Figure 4.10.: The gamma-ray whole sky images with the SNe in the center of the LB. Three different yield masses give the maximum for the gamma-ray line 1809 keV flux from ^{26}Al a medium value and the minimum.

the ^{60}Fe we get a total gamma-ray flux in between $F_{1173\text{keV}/1332\text{keV}} = (0.5 - 22) \cdot 10^{-7}\text{ ph cm}^{-2}\text{ s}^{-1}$, giving the mass input as the biggest uncertainty in the model.

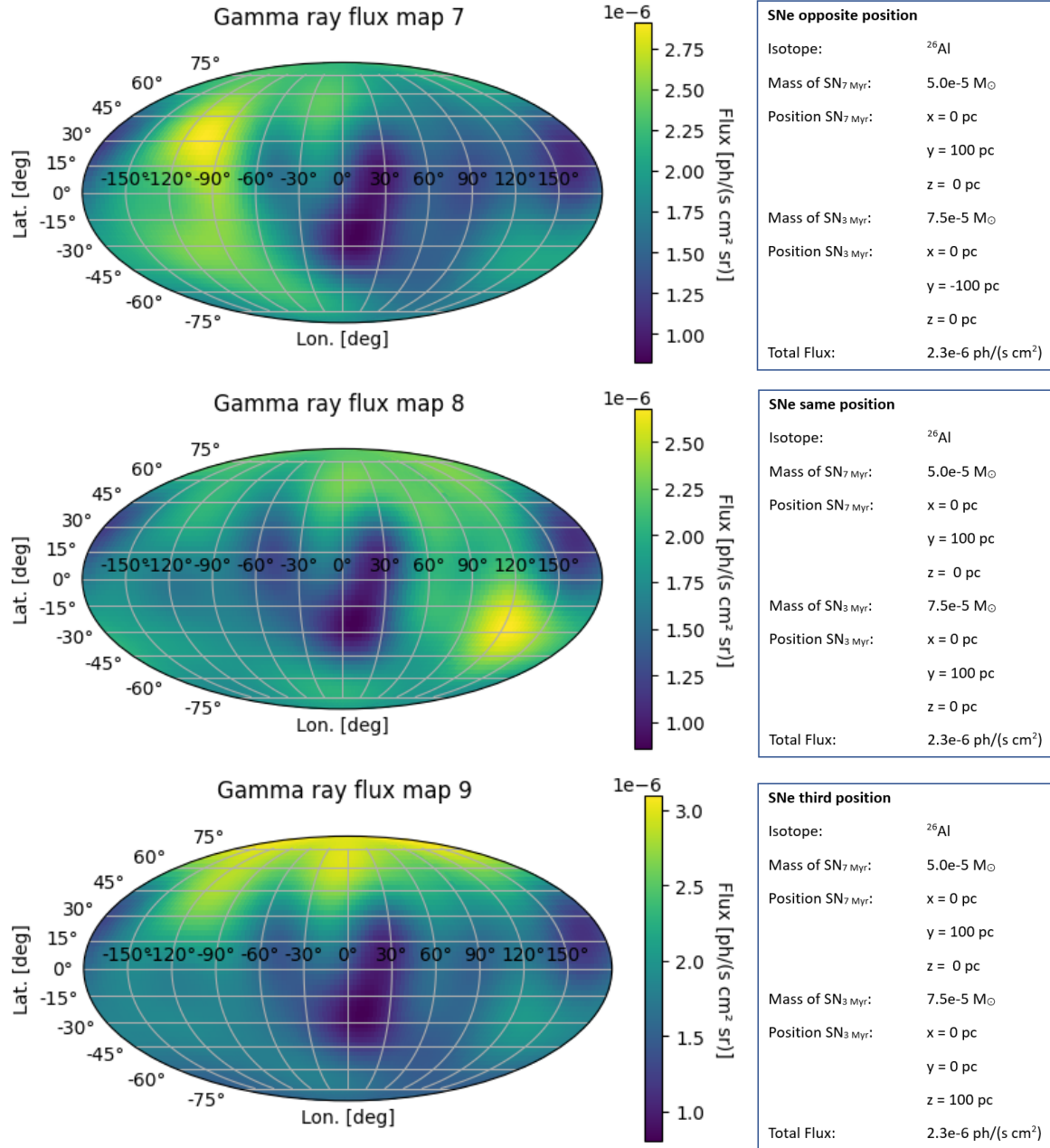


Figure 4.11.: The gamma-ray whole sky images with the SNe at different positions inside of the LB. The mass for the yields of ^{26}Al is a medium value from the possible yields with the considerations above.

Isotropic Contribution

The whole sky imaging of the LB results in an anisotropic emission. However, since the LB is surrounding the Solar System there is an isotropic contribution, e.g. the minimum flux we get from all directions in the sky. Subtracting this value from the flux map results in the purely anisotropic part of the gamma-ray flux. For constellations 1 & 4, this then gives the purely anisotropic emission (total emission minus isotropic emission) in Fig. 4.12, and the total flux is reduced by 50% for the aluminum and reduced by 55% for the iron. The total isotropic gamma-ray line flux for the 1809keV line is $F_{\text{Al, iso}} = 3.2 \cdot 10^{-6} \text{ ph cm}^{-2} \text{ s}^{-1}$ and

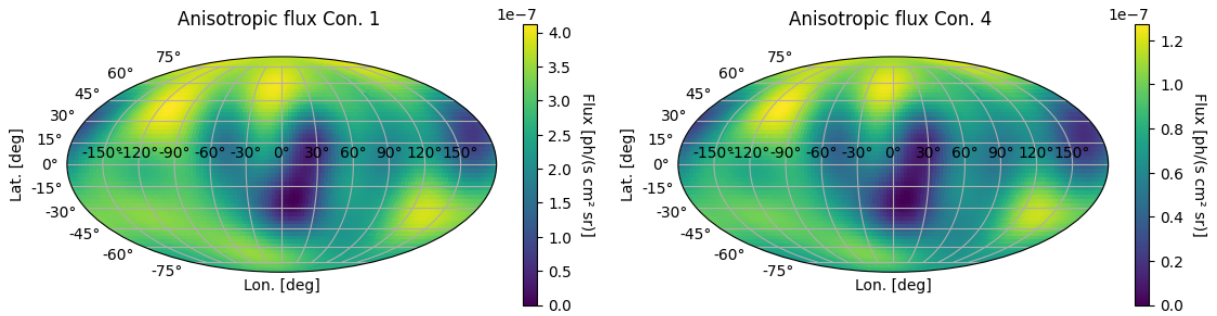


Figure 4.12.: Anisotropic emission of the LB. For ^{26}Al (left) and ^{60}Fe (right). The underlying maps are the result of constellation 1 & 4.

for the 1173keV/1332keV with the input of constellation 4 $F_{\text{Fe, iso}} = 1.9 \cdot 10^{-6} \text{ph cm}^{-2} \text{s}^{-1}$. The isotropic and anisotropic emission from the LB will be discussed in Chp. 6 in the context of the Galactic and the cosmic gamma-ray background.

4.4.1. Distant Superbubble

An additional feature that comes with the model is that we can see how a distant superbubble filled with the same emissivity profile would appear on the whole sky projection. Therefore we simulate a sphere with a radius of 350 pc filled with two SNe at a distance of 800 pc. Inside this sphere, the two SNe sit each with a distance of 100 pc to the center of the sphere on the y-axis in different directions. We do the calculation for SNe that are not time evolved (age would be zero). This explains the total flux in the same order of magnitude as for our LB calculations with $F_{\text{distant}} = 2.10 \cdot 10^{-6} \text{ph s}^{-1} \text{cm}^{-2}$. Adding the time evolution again assuming we have the ^{26}Al gamma-ray line flux to the two SNe gives a total flux of $F_{\text{distant, time}} = 5.87 \cdot 10^{-8} \text{ph s}^{-1} \text{cm}^{-2}$. This shows the impact of the SN remnant age reducing the flux by two orders of magnitude, originating from the exponential decay of 7 Myr and 3 Myr compared to the lifetime of 1 Myr.

The asymmetry in the figure is small but is within the center of the sphere as the flux on the y-axis decays less than on the z-axis. The structure of a sphere and the exponential progress towards the shell is clearly visible. (Fig. 4.13)

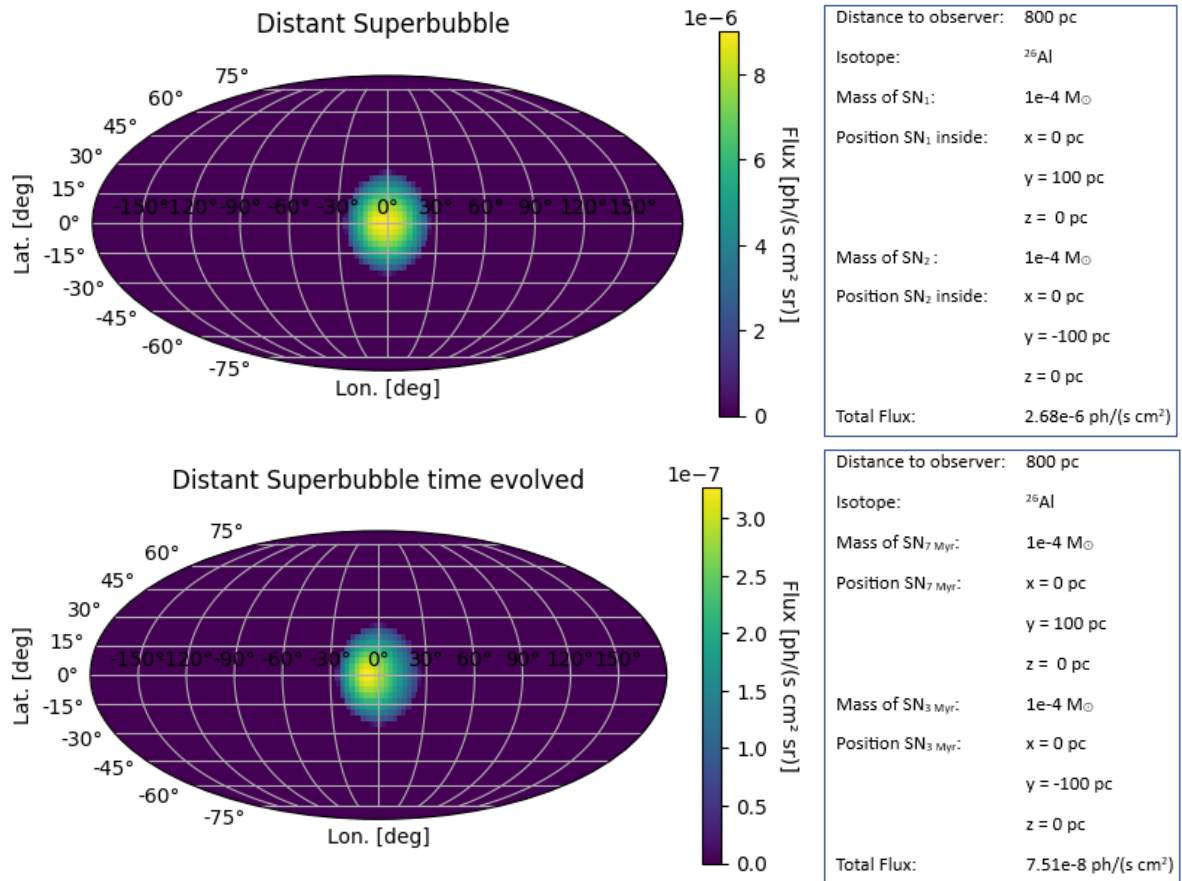


Figure 4.13.: Flux map from an assumed neighboring superbubble in the form of a perfect sphere. Homogenization is ignored.

5. Simulations for the Compton Spectrometer and Imager Satellite Mission

5.1. Compton Spectrometer and Imager

The COMpton Spectrometer and Imager, COSI is NASA's latest small explorer mission (SMEX). It is a gamma-ray telescope, measuring in the soft gamma-ray regime (0.2-5.0 MeV). COSI has a wide field of view with 25% of the sky and covers the whole sky per day. For 511 keV it has an angular resolution of 3.2° (FWHM) and line sensitivity of $(7.9 \cdot 10^{-6} \text{ ph cm}^{-2} \text{ s}^{-1})$, being the 3σ narrow line sensitivity in 2 years of survey observations. And for 1809 keV has an angular resolution of 1.5° (FWHM) and line sensitivity of $(1.7 \cdot 10^{-6} \text{ ph cm}^{-2} \text{ s}^{-1})$ [Tomsick et al., 2019]. COSI will therefore improve the sensitivity in this energy band, compared with COMPTEL and INTEGRAL/SPI (see Fig. 5.1).

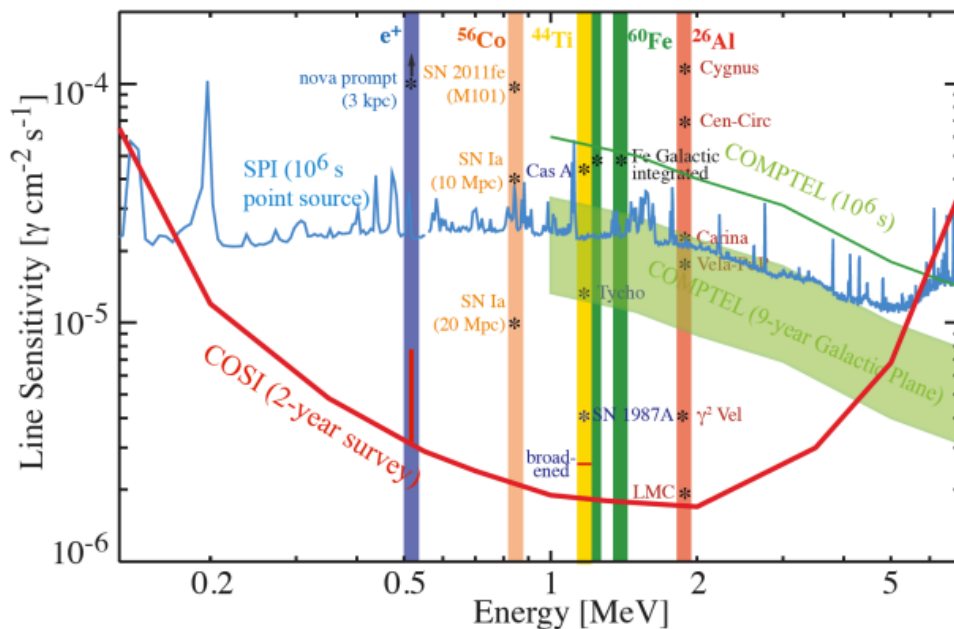


Figure 5.1.: The COSI narrow line sensitivity (3σ) compared with COMPTEL and INTEGRAL/SPI. Figure taken from [Tomsick et al., 2019]

COSI is planned to be active for two years and is a Compton telescope. Compton telescopes use Compton scattering events in the detectors to determine the energy of photons and narrow down the position of the source using the scattering angle for each event. In the energy band where COSI works nuclear reactions happen, it is expected to gain a deeper understanding of nucleosynthesis but also to decipher the origin of Galactic positrons and maybe even detect emission relatable to dark matter [Tomsick et al., 2019]. Proof of concept is also given due to balloon flights with COSI in 2016 [Kierans et al., 2016]. With the structure of the probe and using these balloon flights for calibration, it is possible to simulate different sources if and how COSI would detect them. The current mass model of the telescope (design of 2023) is shown in Fig. 5.2. It is possible that the design might change slightly until the mission will launch, as planned in 2027.

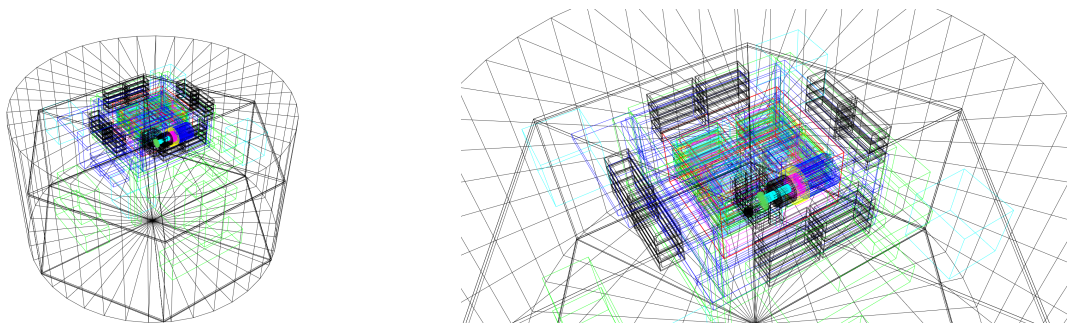


Figure 5.2.: Massmodel of the COSI-SMEX with satellite bus (cylindrical shape), and instrument (colored). The germanium detectors sit in the center of the instrument and are visible as green rectangles in the zoom-in (right).

This setup is used to perform particle-by-particle Monte Carlo simulations with GEANT4-based MEGALib ([Allison et al., 2006], [Zoglauer et al., 2006]). Due to the complexity of these simulations, we use a smaller version of COSI-SMEX for testing purposes called COSERL (see Sec. 5.2). This massmodel reduces the computational effort, as it does not take into account the satellite bus and other additional components. With this, we try to figure out if the LB will be seen in the gamma-ray line of ^{26}Al or ^{60}Fe decay. To do this the flux calculated in section 4 will be used as a source in the simulation.

5.2. Simulations

The simulations are run with the `COSItools`¹. The simulation steps are the following: Needed for the simulations are a source file and a geo setup/massmodel. The former contains the information about the source of the gamma rays namely a flux component. Here, this corresponds to our LB model Sec. 4. It also contains information about the orbit that the satellite has in the simulation and therefore how long measurements take place and when COSI sees what part of the sky. For our case, we use the flux maps that

¹<https://github.com/zoglauer/COSIpy>

are shown in Sec. 4.4 and use an orientation for ca. 25 days of observation time. The geo setup contains information about the detectors, their arrangement, the resulting sensitivity, and other factors due to the different parts of the satellite, i.e. the massmodels for COSI. As mentioned above in our simulations, we use a simplified geometry with respect to the setup shown in Fig. 5.2, called COSERL (Fig. 5.3).

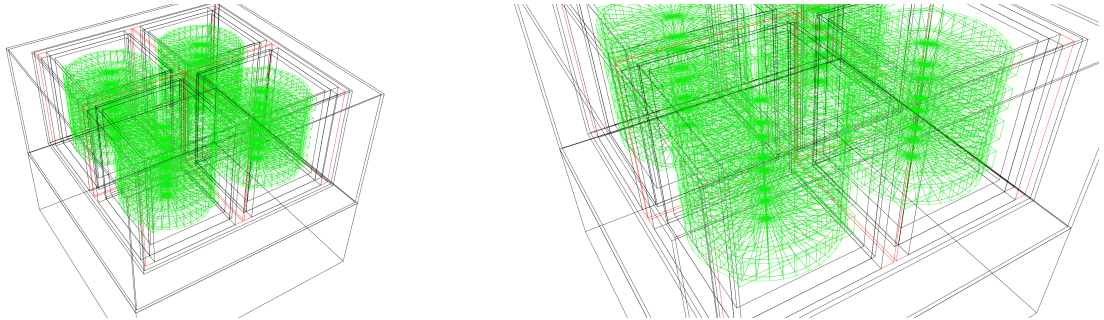


Figure 5.3.: Massmodel for COSERL (left) and zoomed in (right). The detectors sit in the center of the probe (green).

With this, we reduce the computational effort to a manageable time. To do this we need to estimate a scaling factor between the properties of COSERL and COSI-SMEX to mimic the full sensitivity for an exposure time of two years. First, we need to consider the different exposure time spans for the simulation, 25 days, and the planned mission, 2 years. This is given with a linear scaling of:

$$\Delta = \frac{2 \text{ years}}{25 \text{ days}} = \frac{2 \cdot 365.25}{25} = 29.22 \quad (5.1)$$

Then, the effective area of the two massmodels diverges. The relation between the two is given by $A_{\text{COSI-SMEX}}/A_{\text{COSERL}} = 10$ (Zoglauer, priv. comm.), and is later on used as another linear scaling of $\alpha = 10$. This ratio might also depend on the energy, which is estimated to differ by another factor of 2 between COSERL and COSI-SMEX. Other than that, the varying aspect of the COSI-SMEX orbit of $|\pm 22^\circ|$ is not included in the COSERL orbit and might also increase the sensitivity of COSI-SMEX. This however is difficult to estimate without extensive Monte-Carlo simulations, as it probably is a non-linear scaling that depends on the actual source distribution. This latter contribution will be approximated by a scaling factor of $\omega = 2$. It is worth noting that the angular resolution for COSERL is worse than for the COSI-SMEX massmodel, but this would hardly affect the sensitivity in the simulations. All in all, we get a scaling factor for the COSERL 25-day observation to the COSI-SMEX 2-year observation of:

$$f = \Delta \cdot \alpha \cdot \omega = 584.4 \quad (5.2)$$

We will use the scaling factor f , multiplied by the flux maps, in the following simulations

to mimic the actually received counts of photons, with the small-scale setup. We would like to point out once again, that this gives only a rough estimate of how the SMEX might actually perform. Nevertheless, we might obtain a good order of magnitude estimation of the significance with which we expect the LB to be for a two-year or longer observation time.

5.3. Simulation Results

We did the simulations for two gamma-ray flux maps. The model calculated 1809 keV line flux of the LB and the Galactic 1809 keV line flux. For configuration 1 of the LB flux maps and with the described setup for COSERL and the respective scaling, 15171 particles are generated in the first step of the simulation. This then gives 299 reconstructable events, of which 160 are Compton events and result in the spectrum Fig. 5.4 for the LB flux. Doing the same simulation for the whole Galaxy gives 84483 reconstructable events with 48% Compton events and the spectrum also shown in Fig. 5.4. In this figure, for both simulations we recreated an image with the image reconstruction tool *Mimrec*². While we can reconstruct the Galactic plane, as we would expect for the number of counts, the statistics for the LB flux map make it impossible to reconstruct the image with all the structural aspects Fig. 5.4.

If we center a bin around the 1809 keV line with the size of 20 keV we get the counts in this bin for the LB flux map, with 41 counts and the Galaxy map, with 12360 counts. We use these counts to get an idea of how significant the LB is in front of the whole Galaxy. For this we use the following equation for the significance S :

$$S = \frac{C_{LB}}{\sqrt{C_{LB} + C_{MW}}} \cdot \sigma \quad (5.3)$$

With C_{LB} being the total counts of photons in the 1809 keV energy bin from the LB simulation and C_{MW} being the total counts of photons in the 1809 keV energy bin from the MW simulation. Here we, therefore, get a significance of $S = 0.4\sigma$ above the Galactic background. For this value, if our model expectations are correct the contrast of the LB to the Galaxy flux is too small. However, if we consider the structural aspects of the flux whole sky distribution we see a more dominant emission from the LB at higher latitudes compared with the galactic plane (see Chp. 6). Another factor that might worsen the significance estimate even further is that the instrumental background at 1.8 MeV is not included in the calculations above. All in all the significance gives also some estimation for the ^{60}Fe gamma-ray line flux. The LB flux maps for the ^{60}Fe are up to two magnitudes smaller than the one used in the simulation. Therefore we come to the conclusion that we cannot measure the ^{60}Fe lines.

²<https://github.com/zoglauer/COSIPy>

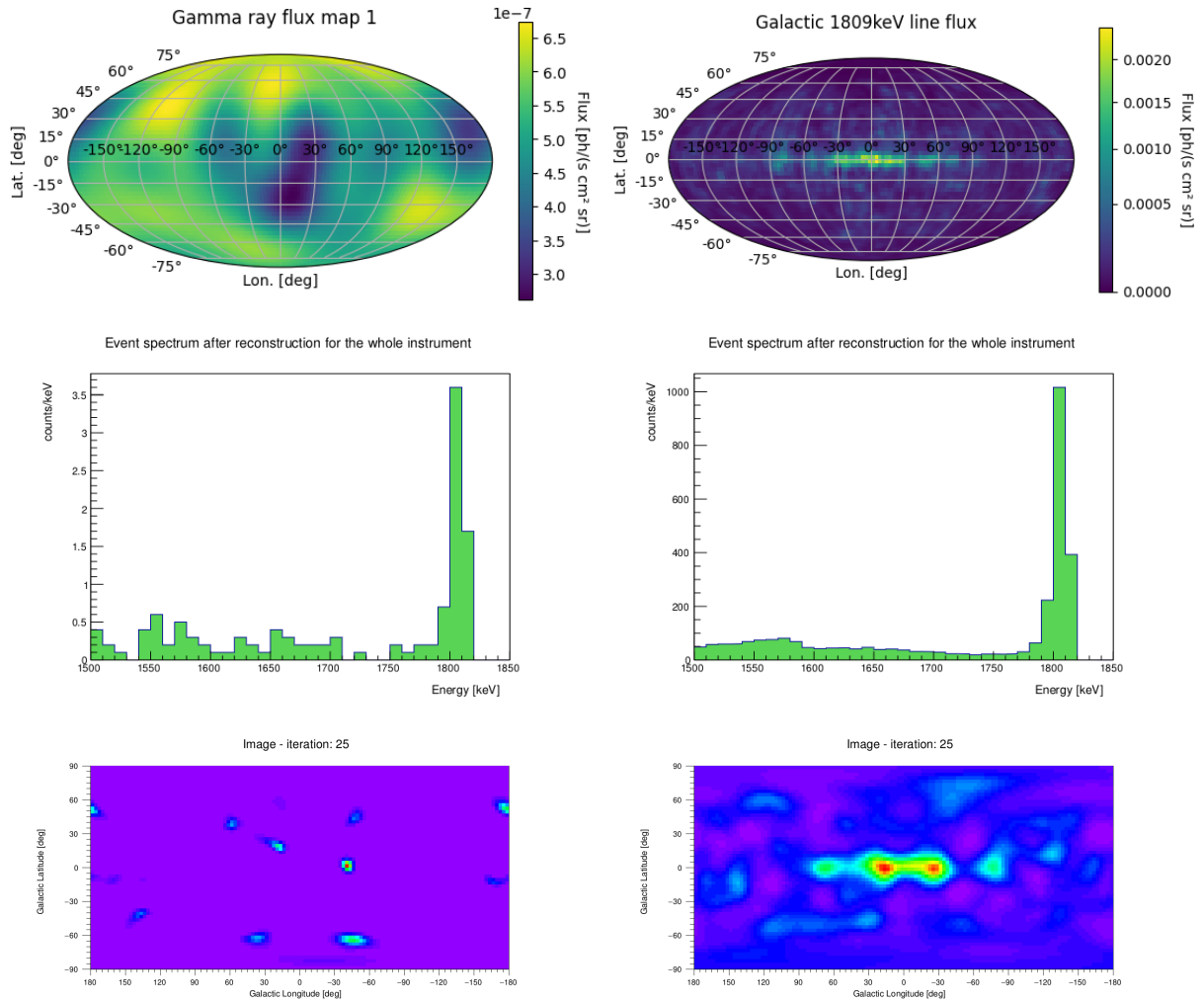


Figure 5.4.: Simulation for the LB gamma-ray flux (left panels) and the Galaxy gamma-ray flux (right panels) for the 1809 keV line of the ^{26}Al decay. The flux maps that are used as the source in the simulation are at the top. The resulting spectra are the middle plots and the image reconstruction is at the bottom. For the Galaxy we can reconstruct the input image with the Galactic plane. For the LB the statistics do not yield enough counts for an image reconstruction.

6. Discussion

6.1. Direct Comparison to Aluminum 26 MW Map

The highest total flux we could produce with the model is $F_{\text{LB,max}} = 6.4 \cdot 10^{-6} \text{ ph cm}^{-2} \text{ s}^{-1}$ for the LB. With the total flux of the MW of $F_{\text{MW}} = 1.8 \cdot 10^{-3} \text{ ph cm}^{-2} \text{ s}^{-1}$ this gives a ratio of $F_{\text{LB}}/F_{\text{MW}} = 0.36\%$. With a line sensitivity of $1.7 \cdot 10^{-6} \text{ ph cm}^{-2} \text{ s}^{-1}$ for the 1809 keV line, of COSI-SMEX this total flux would be within reach. However, the flux is distributed over the whole sky, which results in probably no detection over the 2-year planned observation time of the mission. Nevertheless, due to the structures of the Galactic flux map in contrast to the structure of with our LB model calculated flux maps, some differences show up for which a better ratio is given. To illustrate this, in Fig. 6.1 the relative Flux of the LB to the Galaxy is shown. Here we see that while for the

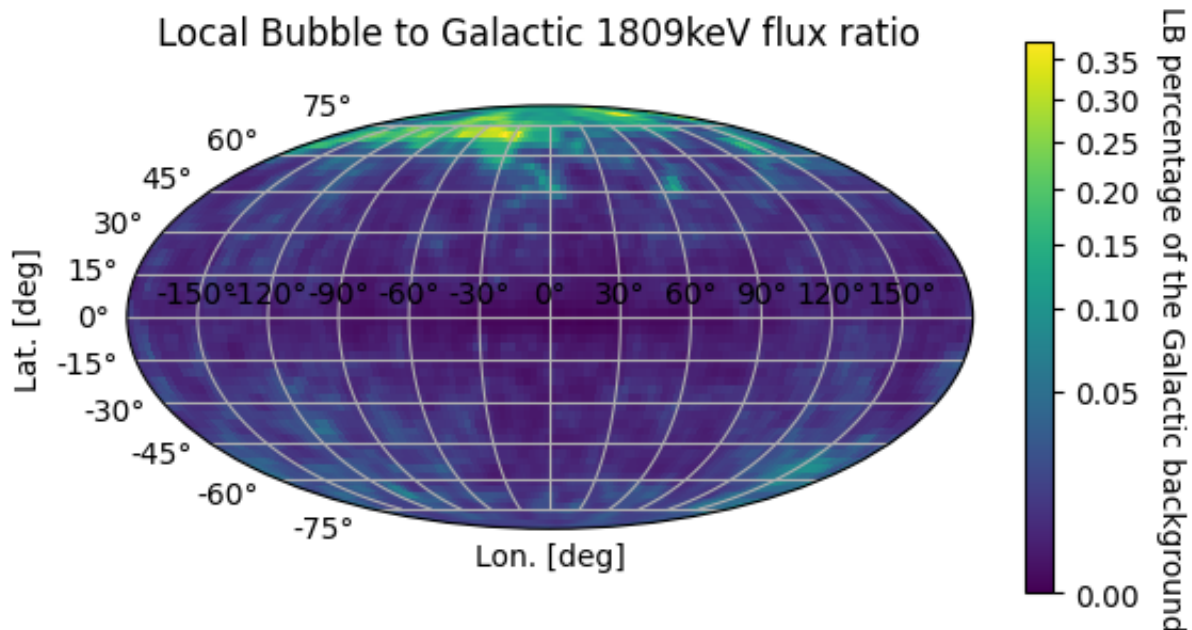


Figure 6.1.: The two previously described flux maps for the Galaxy and the LB model in contrast. In the Galactic plane, the contribution to the Flux from the LB is zero in front of the background. For high latitudes, the Contribution of the LB reaches up to 35%

Galactic plane, the LB contribution is not visible, for higher latitudes the LB makes up for up to 35% of the flux coming from that part of the sky. Therefore these high latitudes

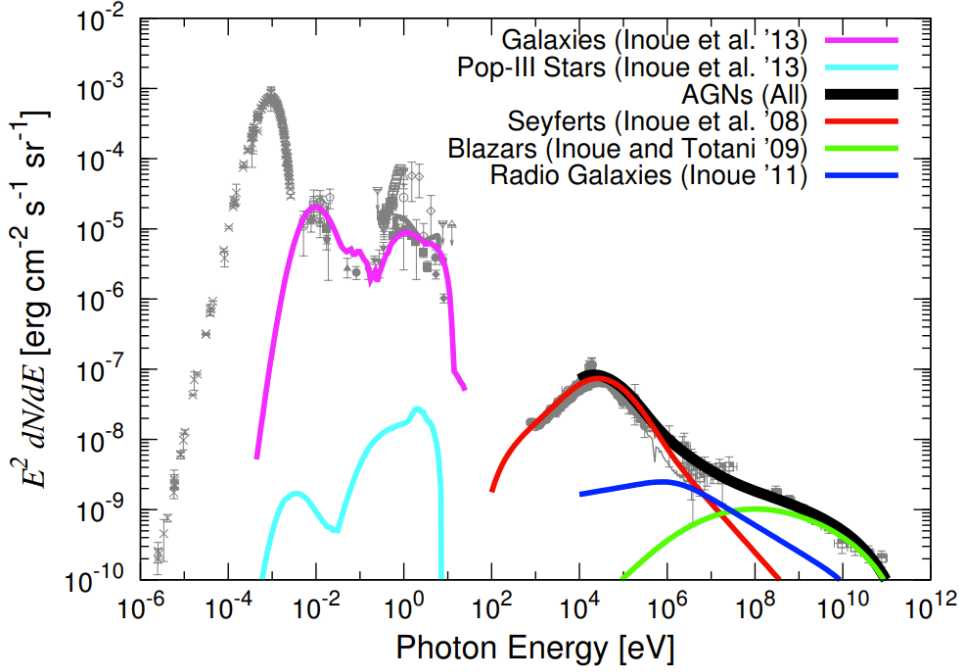


Figure 6.2.: The cosmic radiation background, for microwaves up to gamma rays. Figure taken from [Inoue, 2014]

are preferable in the attempt of measuring the LB gamma-ray line flux. COSI-SMEX differs from previous missions with its focus on the whole sky. As mentioned COSI will cover the whole sky during one orbit with its wide field of view of 25 %. Therefore with COSI-SMEX, there is a higher chance to detect the high-latitude regions where the LB flux becomes more dominant in the total flux distribution.

6.2. Cosmic Gamma Ray Background Lines

Besides the SNe lines with high redshift, we can estimate to what part the nucleosynthesis lines of intermediate lifetime elements ^{26}Al and ^{60}Fe contribute to the CGB. The cosmic radiation background is shown in Fig. 6.2. To compare the model expected flux for the LB with the plotted spectrum we need to describe the respective gamma-ray line with a Gaussian. For this we again take the flux for the 1809keV line $F_{\text{LB},1809\text{keV}} = 6.4 \cdot 10^{-6} \text{ ph cm}^{-2} \text{ s}^{-1}$ and the flux for the 1173keV line $F_{\text{LB},1173\text{keV}} = 1.1 \cdot 10^{-6} \text{ ph cm}^{-2} \text{ s}^{-1}$ (representative for both ^{60}Fe gamma-ray lines). We assume the line width to be 1.8 keV for the 1809 keV line and 1.2 keV for the 1173 keV line, this corresponds to the redshift at the sound speed we used earlier in the calculations. The Gaussian then reads:

$$\text{Gaussian} = \frac{F}{\sqrt{2\pi}\sigma} \cdot \exp\left(-\frac{E - 1809\text{keV}}{2\sigma^2}\right) \quad (6.1)$$

With F the model calculated flux σ the line width. This gives us a spectrum, which we can adapt to the one used for the CGB in Fig. 6.2. The Maximum of the two spectra then reads for the 1809keV line $\text{Max}_{1809\text{keV}} = 5.8 \cdot 10^{-10} \text{ erg cm}^{-2} \text{ s}^{-1} \text{ sr}^{-1}$ and for the 1173 keV line $\text{Max}_{1173\text{keV}} = 6.4 \cdot 10^{-11} \text{ erg cm}^{-2} \text{ s}^{-1} \text{ sr}^{-1}$. With this, the ^{26}Al line is about a factor of 20 (200 for the ^{60}Fe line) smaller than the surrounding continuum for AGN, however, with the total flux confined in a single gamma-ray line it is possible to distinguish these.

7. Conclusion

In this thesis, the hypothesis of an isotropic contribution of gamma-ray lines to the cosmic gamma-ray background was examined.

For two nearby supernovae, within the Local Bubble, we model calculate the gamma-ray line flux of two radioactive isotopes ^{26}Al and ^{60}Fe at the position of the Solar System. For this, with given yield calculations from [Limongi and Chieffi, 2018], the mass, rotating velocity, and metallicity are taken into account. From [Chaikin et al., 2022] the supernovae are dated recently with 3 and 7 Myr ago. We find that stars of the masses 13 - 25 M_{\odot} exploded, giving potential ^{26}Al -yields of $M_{\text{Al26}} = (1.55 - 13.7) \cdot 10^{-5} M_{\odot}$ and ^{60}Fe -yields of $M_{\text{Fe60}} = (0.08 - 5.0) \cdot 10^{-5} M_{\odot}$. The uncertainties result from the assumptions of how fast the progenitor stars could have been rotating and also from two different approaches to estimate the metallicity of the progenitor stars. The latter has a large impact, especially on the iron yield.

For the structure of the Local Bubble, Line of Sight integration from an observer up to the shell given by [Pelgrims, V. et al., 2020] gives the model calculated flux for an assumed emissivity profile. The emissivity profile takes into account the position of these recent supernovae, the sound speed in the Local Bubble, the yields of radioactive isotopes ^{60}Fe and ^{26}Al , and the age of the supernovae.

This results in flux at the 1809 keV line of ^{26}Al in the range of $F_{\text{Al26}} = (0.73 - 6.4) \cdot 10^{-6} \text{ ph cm}^{-2} \text{ s}^{-1}$ with an isotropic contribution of 50% and flux at the 1173/1332 keV line in the range of $F_{\text{Fe60}} = (0.45 - 22) \cdot 10^{-7} \text{ ph cm}^{-2} \text{ s}^{-1}$ with an isotropic contribution of 54% for the Local Bubble.

Current telescopes namely INTEGRAL/SPI and COMPTEL can not measure this flux at the moment. In the future, the small explorer mission COSI might see the contrast to the Galactic background that is given for higher latitudes in Galactic coordinates. We performed whole sky simulations with a simplified massmodel for COSI for the observation time of 2 years, which gave a detection significance below 3σ . Again the Local Bubble flux map deviations from the Galactic background in high latitudes could provide a possibility to be distinguished with sufficient analysis.

The gamma-ray narrow line contribution of ^{26}Al is on the order of 5% at 1809 keV to the cosmic gamma-ray background and for ^{60}Fe at 1173/1332 keV 0.5% to the cosmic gamma-ray background. The wide field of view and the observation along the ecliptic of COSI ensure, that more exposure is spent on higher latitudes. This might also make it

possible to distinguish the isotropic gamma-ray line contribution from the background of the Galactic plane and the continuum from AGN in the cosmic gamma-ray background.

Bibliography

- [Allison et al., 2006] Allison, J., Amako, K., Apostolakis, J., Araujo, H., Dubois, P. A., Asai, M., Barrand, G., Capra, R., Chauvie, S., Chytracsek, R., Cirrone, G. A. P., Cooperman, G., Cosmo, G., Cuttone, G., Daquino, G. G., Donszelmann, M., Dressel, M., Folger, G., Foppiano, F., Generowicz, J., Grichine, V., Guatelli, S., Gumplinger, P., Heikkinen, A., Hrivnacova, I., Howard, A., Incerti, S., Ivanchenko, V., Johnson, T., Jones, F., Koi, T., Kokoulin, R., Kossov, M., Kurashige, H., Lara, V., Larsson, S., Lei, F., Link, O., Longo, F., Maire, M., Mantero, A., Mascialino, B., McLaren, I., Lorenzo, P. M., Minamimoto, K., Murakami, K., Nieminen, P., Pandola, L., Parlati, S., Peralta, L., Perl, J., Pfeiffer, A., Pia, M. G., Ribon, A., Rodrigues, P., Russo, G., Sadilov, S., Santin, G., Sasaki, T., Smith, D., Starkov, N., Tanaka, S., Tcherniaev, E., Tome, B., Trindade, A., Truscott, P., Urban, L., Verderi, M., Walkden, A., Wellisch, J. P., Williams, D. C., Wright, D., and Yoshida, H. (2006). Geant4 developments and applications. *IEEE Transactions on Nuclear Science*, 53(1):270–278.
- [Breitschwerdt et al., 2016] Breitschwerdt, D., Feige, J., Schulreich, M. M., Avillez, M. A. D., Dettbarn, C., and Fuchs, B. (2016). The locations of recent supernovae near the Sun from modelling ^{60}Fe transport. , 532(7597):73–76.
- [Chaikin et al., 2022] Chaikin, E., Kaurov, A. A., Fields, B. D., and Correa, C. A. (2022). Simulations of ^{60}Fe entrained in ejecta from a near-Earth supernova: effects of observer motion. , 512(1):712–727.
- [Cheng et al., 2012] Cheng, J. Y., Rockosi, C. M., Morrison, H. L., Schönrich, R. A., Lee, Y. S., Beers, T. C., Bizyaev, D., Pan, K., and Schneider, D. P. (2012). Metallicity Gradients in the Milky Way Disk as Observed by the SEGUE Survey. , 746(2):149.
- [Diehl et al., 1995] Diehl, R., Dupraz, C., Bennett, K., Bloemen, H., Hermsen, W., Knoedlseder, J., Lichti, G., Morris, D., Ryan, J., Schönfelder, V., Steinle, H., Strong, A., Swanenburg, B., Varendorff, M., and Winkler, C. (1995). Comptel observations of galactic ^{26}Al emission. *p*, 298 : 445.
- [Ellis and Schramm, 1995] Ellis, J. and Schramm (1995). Could a nearby supernova explosion have caused a mass extinction? *Proceedings of the National Academy of Sciences of the United States of America*, 92(1):235–238.
- [Glebocki and Gnacinski, 2005] Glebocki, R. and Gnacinski, P. (2005). VizieR Online Data Catalog: Catalog of Stellar Rotational Velocities (Glebocki+ 2005). *VizieR Online Data Catalog*, page III/244.

- [GRAVITY Collaboration et al., 2019] GRAVITY Collaboration, Abuter, R., Amorim, A., Bauböck, M., Berger, J. P., Bonnet, H., Brandner, W., Clénet, Y., Coudé Du Foresto, V., de Zeeuw, P. T., Dexter, J., Duvert, G., Eckart, A., Eisenhauer, F., Förster Schreiber, N. M., Garcia, P., Gao, F., Gendron, E., Genzel, R., Gerhard, O., Gillessen, S., Habibi, M., Haubois, X., Henning, T., Hippler, S., Horrobin, M., Jiménez-Rosales, A., Jocou, L., Kervella, P., Lacour, S., Lapeyrère, V., Le Bouquin, J. B., Léna, P., Ott, T., Paumard, T., Perraut, K., Perrin, G., Pfuhl, O., Rabien, S., Rodriguez Coira, G., Rousset, G., Scheithauer, S., Sternberg, A., Straub, O., Straubmeier, C., Sturm, E., Tacconi, L. J., Vincent, F., von Fellenberg, S., Waisberg, I., Widmann, F., Wiegrecht, E., Wiezorrek, E., Woillez, J., and Yazici, S. (2019). A geometric distance measurement to the Galactic center black hole with 0.3% uncertainty. , 625:L10.
- [Inoue, 2014] Inoue, Y. (2014). Cosmic Gamma-ray Background Radiation. *arXiv e-prints*, page arXiv:1412.3886.
- [Jaeck,] Jaeck, A. Internetchemie isotope. <https://www.internetchemie.info/>. Accessed: 11.05.2023.
- [Kierans et al., 2016] Kierans, C., Boggs, S., Chiu, J. L., Lowell, A., Sleator, C., Tomsick, J. A., Zoglauer, A., Amman, M., Chang, H. K., Tseng, C. H., Yang, C. Y., Lin, C. H., Jean, P., and von Ballmoos, P. (2016). The 2016 Super Pressure Balloon flight of the Compton Spectrometer and Imager. In *11th INTEGRAL Conference Gamma-Ray Astrophysics in Multi-Wavelength Perspective*, page 75.
- [Krause et al., 2014] Krause, M., Diehl, R., Böhringer, H., Freyberg, M., and Lubos, D. (2014). Feedback by massive stars and the emergence of superbubbles. II. X-ray properties. , 566:A94.
- [Krause et al., 2018] Krause, M. G. H., Burkert, A., Diehl, R., Fierlinger, K., Gaczkowski, B., Kroell, D., Ngoumou, J., Roccatagliata, V., Siebert, T., and Preibisch, T. (2018). Surround and Squash: the impact of superbubbles on the interstellar medium in Scorpius-Centaurus OB2. , 619:A120.
- [Limongi and Chieffi, 2018] Limongi, M. and Chieffi, A. (2018). Presupernova Evolution and Explosive Nucleosynthesis of Rotating Massive Stars in the Metallicity Range $-3 \leq [\text{Fe}/\text{H}] \leq 0$. , 237(1):13.
- [Lugaro and Chieffi, 2011] Lugaro, M. and Chieffi, A. (2011). Radioactivities in Low- and Intermediate-Mass Stars. In Diehl, R., Hartmann, D. H., and Prantzos, N., editors, *Lecture Notes in Physics, Berlin Springer Verlag*, volume 812, pages 83–152.
- [Pelgrims, V. et al., 2020] Pelgrims, V., Ferrière, K., Boulanger, F., Lallement, R., and Montier, L. (2020). Modeling the magnetized local bubble from dust data. *A&A*, 636:A17.

- [Pleintinger, 2020] Pleintinger, M. M. M. (2020). *Star Groups and their Nucleosynthesis*. PhD thesis, Technische Universität München.
- [Pleintinger et al., 2023] Pleintinger, M. M. M., Diehl, R., Siegert, T., Greiner, J., and Krause, M. G. H. (2023). ^{26}Al gamma rays from the Galaxy with INTEGRAL/SPI. , 672:A53.
- [Siegert, 2017] Siegert, T. (2017). *Positron-Annihilation Spectroscopy throughout the Milky Way*. Dissertation, Technische Universität München, München.
- [Siegert et al., 2022] Siegert, T., Bertheaud, J., Calore, F., Serpico, P. D., and Weinberger, C. (2022). Diffuse Galactic emission spectrum between 0.5 and 8.0 MeV. , 660:A130.
- [Tomsick et al., 2019] Tomsick, J., Zoglauer, A., Sleator, C., Lazar, H., Beechert, J., Boggs, S., Roberts, J., Siegert, T., Lowell, A., Wulf, E., Grove, E., Philips, B., Brandt, T., Smale, A., Kierans, C., Burns, E., Hartmann, D., Leising, M., Ajello, M., Fryer, C., Amman, M., Chang, H.-K., Jean, P., and von Ballmoos, P. (2019). The Compton Spectrometer and Imager. In *Bulletin of the American Astronomical Society*, volume 51, page 98.
- [Wallner et al., 2021] Wallner, A., Froehlich, M. B., Hotchkis, M. A. C., Kinoshita, N., Paul, M., Martschini, M., Pavetich, S., Tims, S. G., Kivel, N., Schumann, D., Honda, M., Matsuzaki, H., and Yamagata, T. (2021). ^{60}Fe and ^{244}Pu deposited on Earth constrain the r-process yields of recent nearby supernovae. *Science*, 372(6543):742–745.
- [Wang et al., 2007] Wang, W., Harris, M. J., Diehl, R., Halloin, H., Ciemniak, C., Strong, A. W., and Kretschmer, K. (2007). ^{60}Fe Studies with INTEGRAL’s Spectrometer SPI. In *The Obscured Universe. Proceedings of the VI INTEGRAL Workshop*, volume 622 of *ESA Special Publication*, page 77.
- [Wang et al., 2020] Wang, W., Siegert, T., Dai, Z. G., Diehl, R., Greiner, J., Heger, A., Krause, M., Lang, M., Pleintinger, M. M. M., and Zhang, X. L. (2020). Gamma-Ray Emission of ^{60}Fe and ^{26}Al Radioactivity in Our Galaxy. , 889(2):169.
- [Woosley et al., 2002] Woosley, S. E., Heger, A., and Weaver, T. A. (2002). The evolution and explosion of massive stars. *Reviews of Modern Physics*, 74(4):1015–1071.
- [Zoglauer et al., 2006] Zoglauer, A., Andritschke, R., and Schopper, F. (2006). MEGALib The Medium Energy Gamma-ray Astronomy Library. , 50(7-8):629–632.
- [Zucker et al., 2022] Zucker, C., Goodman, A. A., Alves, J., Bialy, S., Foley, M., Speagle, J. S., Großschedl, J., Finkbeiner, D. P., Burkert, A., Khimey, D., and Swiggum, C. (2022). Star formation near the Sun is driven by expansion of the Local Bubble. , 601(7893):334–337.

A. Appendix

On the following pages, the code that was used for the flux calculations and other interim results is shown. Also, supplementary figures can be found.

A.1. Model Programming

The heart of the program is the LOS function. This is where the parametrization of the LOS, the inclusion of the shell of the LB, as well as the position of the SNe with the resulting profile takes place.

Listing A.1: LOS-function

```
import numpy as np
from numba import jit , prange
from numpy import cos , sin , exp , pi , arccos , arctan
import matplotlib.pyplot as plt
import time
import astropy.units as u
import astropy.constants as c
@jit(nopython=True)
def LOS(s: float , phi: float , theta: float) -> float:

    x = x0 + s * cos(np.pi /180 * phi) * cos(np.pi /180 * theta)
    y = y0 + s * sin(np.pi /180 * phi) * cos(np.pi /180 * theta)
    z = z0 + s * sin(np.pi /180 * theta)

    r = np.sqrt((x - xm)**2 + (y - ym)**2 + (z - zm)**2)

    dp1 = np.sqrt((x - xp1) ** 2 + (y - yp1) ** 2 + (z - zp1) ** 2)
    dp2 = np.sqrt((x - xp2) ** 2 + (y - yp2) ** 2 + (z - zp2) ** 2)

    Rk = R(phi , theta)
    if r <= Rk:
        return
        Alu*(S1Alt*exp(-dp1*ab))/(4*np.pi)
```

```

+ S2Alt*exp(-dp2*ab)/(4*np.pi) +
Fe*(S1Fet*exp(-dp1*ab2)/(4*np.pi)
+ S2Fet*exp(-dp2*ab2)/(4*np.pi)
else:
return 0

```

Python: Used packages `numpy`¹, `matplotlib`², `numba`³, and `astropy`⁴. The first part of the function is the parametrization of the LOS, in spherical coordinates. Then the distance from the observer r and the distances to the SNe d is implemented. After that, the array $R(\phi, \theta)$ is evaluated for the given solid angle. The return of the function then is either the contribution to the flux in a point on the LOS (inside LB) or 0 (outside LB). `S1Alt` and `S2Alt` are the time-developed emissivities for the two SNe.

Listing A.2: Input-parameters

```

#Aluminum26
##Probability
p = 1
##Atomic mass
m = 25.986891867 * c.u
##Decay constant
tau = 3.065488822009e-14*(1/tNorm)

#Iron60
##Probability
p2 = 1
##Atomic mass
m2 = 59.9340704 * c.u
##Decay constant
tau2 = 8.389142331942e-15 *(1/tNorm)

#####

#Mass
Minput1 = 1e-4 *c.M_sun
Minput2 = 1e-4 *c.M_sun
Minput3 = 0.08e-5 *c.M_sun
Minput4 = 0.2e-5 *c.M_sun

```

¹<https://numpy.org/>

²<https://matplotlib.org/>

³<https://numba.pydata.org/>

⁴<https://docs.astropy.org/>

```
#Age
t1input = 3e6 * u.year
t2input = 7e6 * u.year
t3input = 3e6 * u.year
t4input = 7e6 * u.year
```

First the properties of ^{26}Al and ^{60}Fe as shown in table 4.1 are implemented and then the input parameters for the SNe with the ending on 1 or 2 corresponding to the two SNe in ^{26}Al and ending on 3 or 4 the two SNe in ^{60}Fe . The used packages are the same as before.

```
Effective Volume:                26451265.378401946 pc3
Machine time profile:            27.697998762138737 s
Emissivity1Al:                  1.1210784409404473e-20 1 / (m3 s)
Emissivity2Al:                  1.644390654349297e-22 1 / (m3 s)
Machine time Riemann:            9.413295030593872 s
Total Flux via Monte-Carlo Al26: 5.365555296449676e-06 1 / (cm2 s)
Total Flux via Riemann-Summe Al 26: 5.370996711792021e-06 1 / (cm2 s)
Luminosity1 Aluminium:          8.712325431378155e+36 1 / s
Luminosity2 Aluminium:          1.277918296688481e+35 1 / s
Machine time Monte-Carlo:        24.42870569229126 s

Process finished with exit code 0
```

Figure A.1.: Output of the model for the parameters used in ??.

A.2. Additional Figures

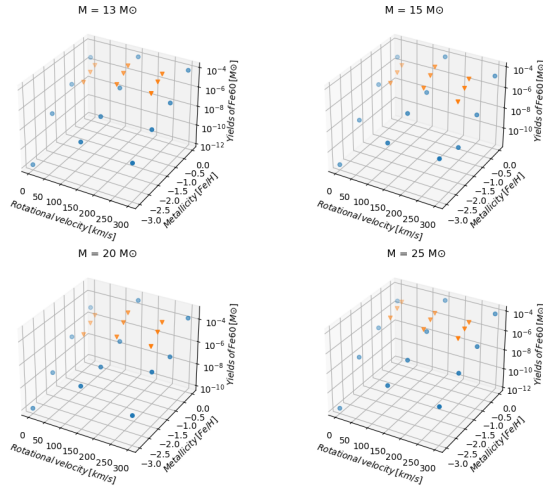


Figure A.2.: Yields of ^{60}Fe (blue) supplemented with the interpolated values at the determined rotational velocities and metallicities (orange). The interpolation works linearly between the given values for the yields.

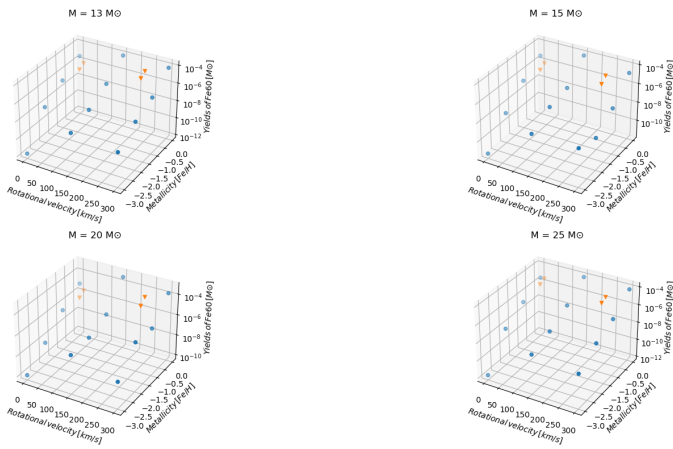


Figure A.3.: Yields of ^{60}Fe (blue) supplemented with the interpolated values at the end of a $1\text{-}\sigma$ velocity band and the two highest metallicities (orange). The interpolation works linearly between the given values for the yields.

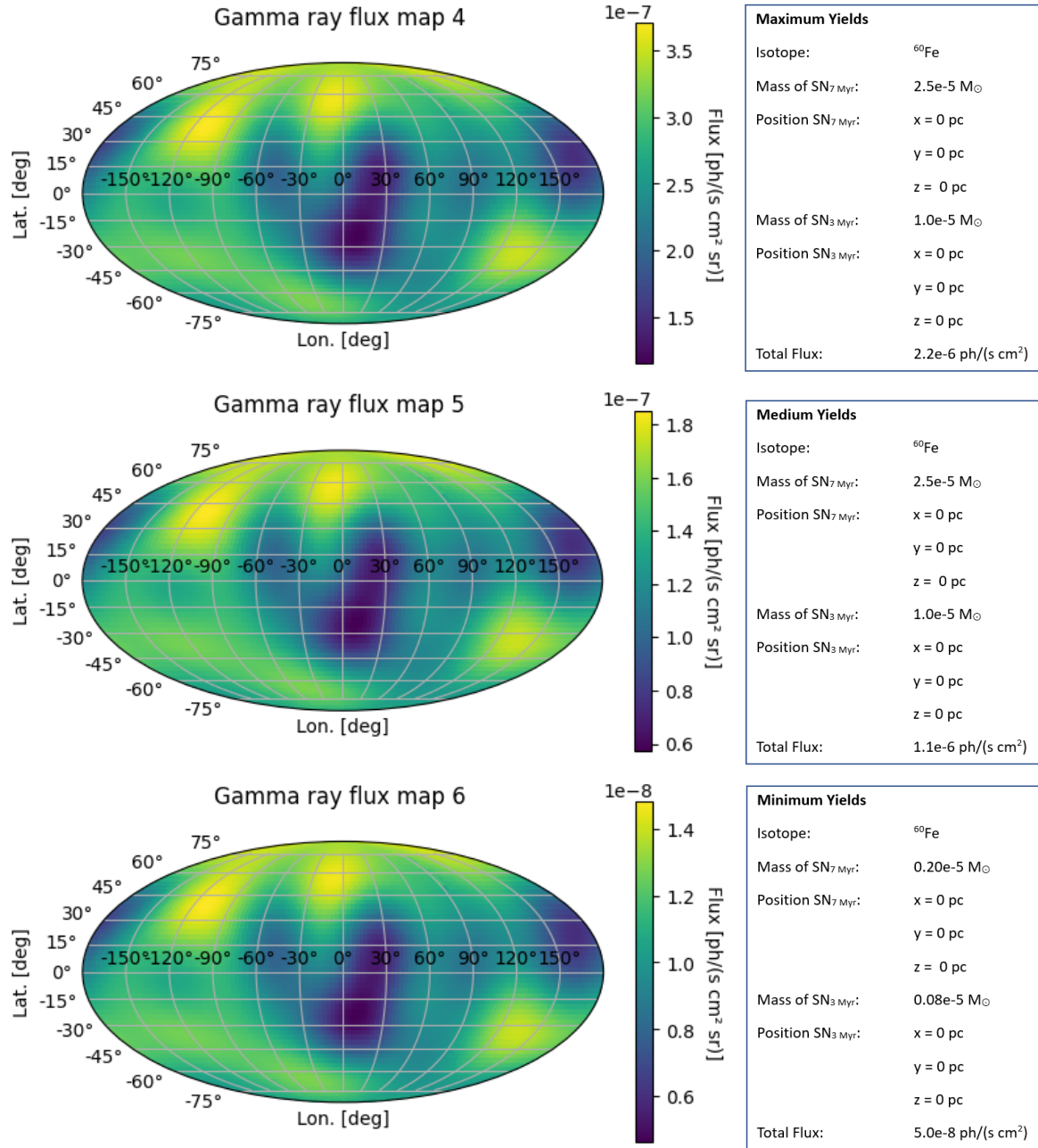


Figure A.4.: The gamma-ray whole sky images with the SNe in the center of the LB. Three different yield masses give the maximum for the gamma-ray line 1173/1332 keV flux from ^{60}Fe . The yields correspond to the two metallicity approaches.

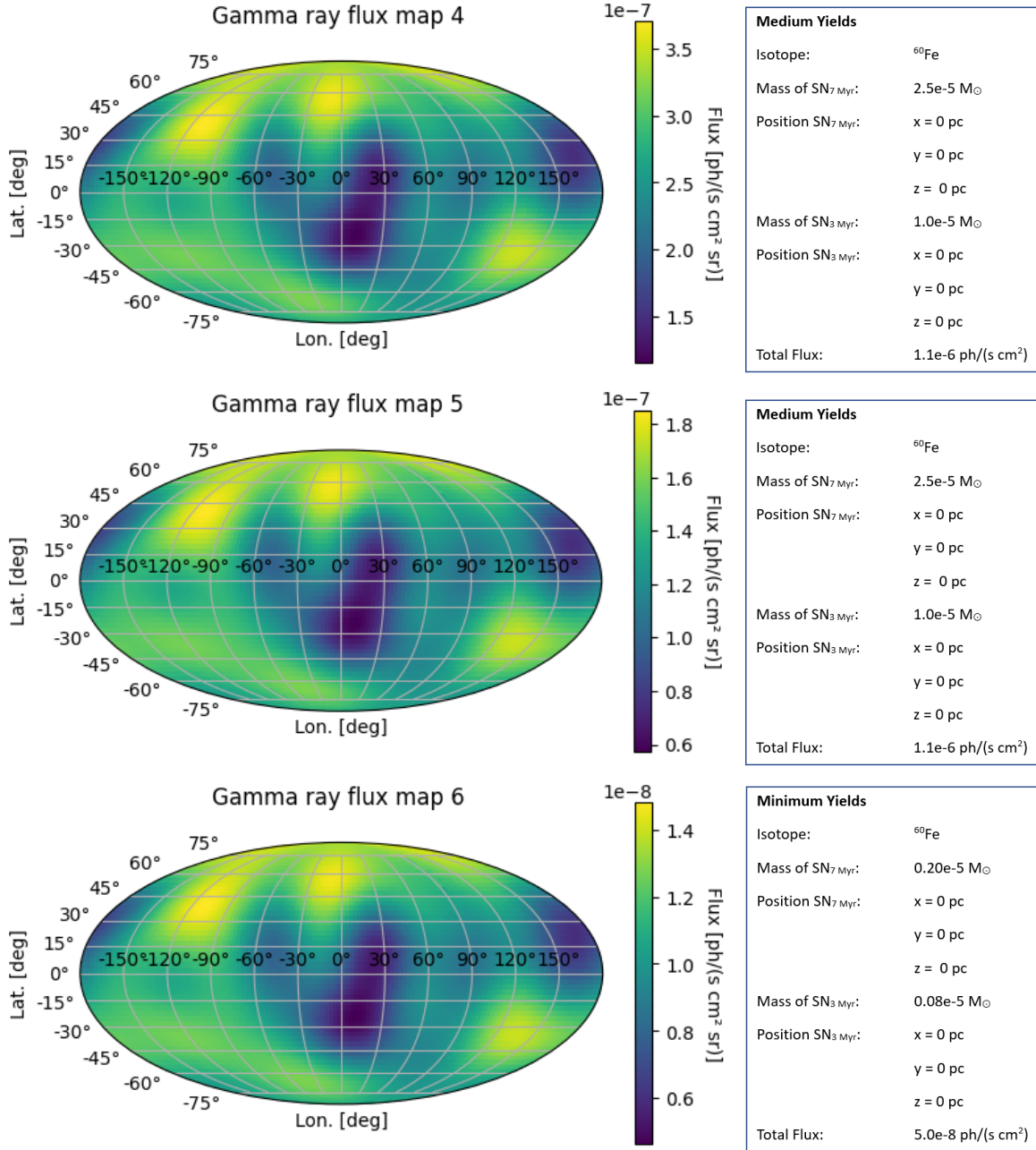


Figure A.5.: The gamma-ray whole sky images with the SNe at different positions inside of the LB. The mass for the yields of ⁶⁰Fe is the result for the supersolar metallicity and a propagation/efficiency coefficient of $f_{\text{Fe},60} = 0.004$.

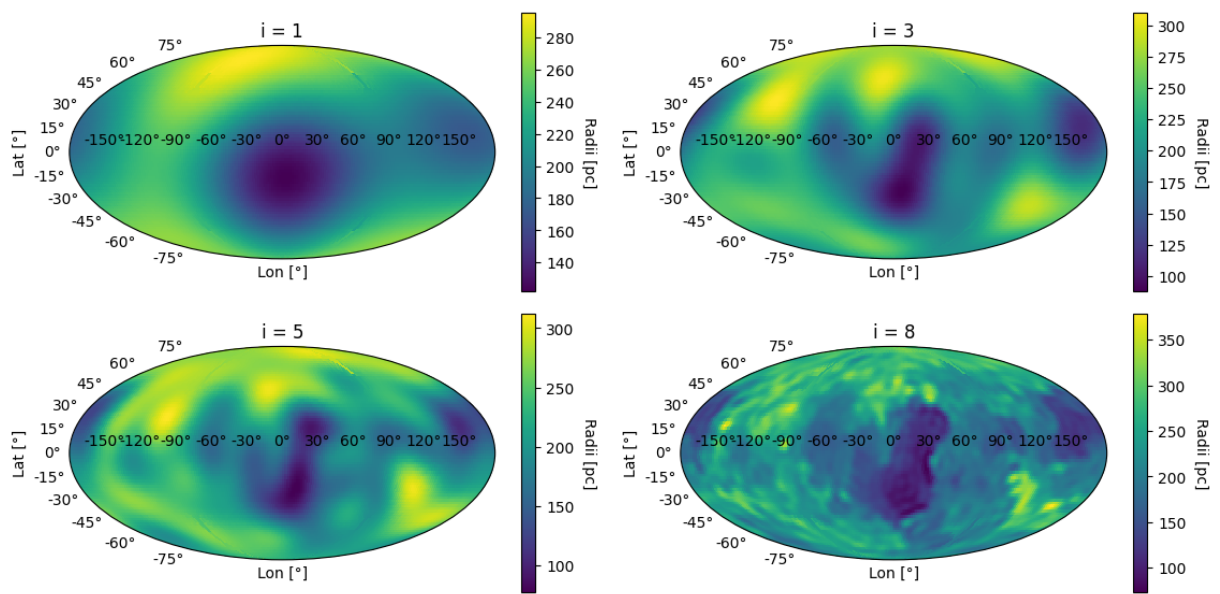
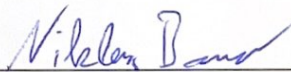


Figure A.6.: Gamma ray flux whole sky imaging for the different complexities of the Local Bubble shell. The images are the result of the model for $i = \{1; 3; 5; 8\}$. The total flux for $i = 1$ is $4.89\text{e-}6$ and for $i = 8$ is $4.71\text{e-}6$

Eidesstattliche Erklärung

Hiermit erkläre ich, dass ich die vorliegende Arbeit eigenständig und ohne fremde Hilfe angefertigt habe. Textpassagen, die wörtlich oder dem Sinn nach auf Publikationen oder Vorträgen anderer Autoren beruhen, sind als solche kenntlich gemacht. Die Arbeit wurde bisher keiner anderen Prüfungsbehörde vorgelegt und auch noch nicht veröffentlicht.

Würzburg, 16.06.2023


Niklas Bauer